Renewable Energy 206 (2023) 722–737

Contents lists available at ScienceDirect

Renewable Energy

journal homepage: www.elsevier.com/locate/renene

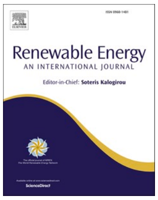

Modelling analysis of a solar-driven thermochemical energy storage unit combined with heat recovery

Yong Zhang, Mingke Hu [*], Ziwei Chen, Yuehong Su [**], Saffa Riffat

Department of Architecture and Built Environment, University of Nottingham, University Park, Nottingham, NG7 2RD, UK

ARTICLE INFO

Keywords:
Thermochemical energy storage
Solar energy
Solar photovoltaic/thermal
Heat recovery
Composite materials

ABSTRACT

Solar-driven thermochemical energy storage (TCES) can address the mismatch between solar heat production and heating demand and contribute to decarbonisation in buildings. In many studies of typical salt hydrate TCES systems, massive heat carried by the discharged humid airflow during the charging phase is not well-utilised but directly dissipated to the ambient. Therefore, a solar photovoltaic/thermal-powered TCES system integrating a heat exchanger (PV/T-TCES-HEX system) is proposed in this study for recovering this part of heat. To study the effect of adding the PV/T collector and heat exchanger (HEX) on the performance of the TCES system, the thermal performance of the PV/T-TCES-HEX system is compared with other two TCES systems via COMSOL modelling. Results suggest that the PV/T-TCES-HEX system requires an additional external electricity input of 11.86 kWh on a typical summer day in Nottingham, which is only 40.53% of the TCES-only system. The overall thermal efficiency of the PV/T-TCES-HEX system is 56.00%, indicating an efficiency enhancement of 146.80%. A lower mass flow rate leads to higher thermal efficiency and storage energy. The system has the highest overall thermal efficiency when the reactor bed thickness is 0.04 m (57.55%) and when the reactor bed length is 0.5 m (58.73%).

1. Introduction

The world total energy consumption has maintained continuous growth in the last 20 years because of population growth and accelerated industrialisation. The global primary energy consumption in 2021 was 5.95 × 10^{11} MJ, an increase of 51% compared to 2000 [1]. In the UK, the residential sector consumes nearly one-third of the total energy supply, and heating systems account for 83% of residential sector energy consumption [2,3]. The energy crisis the UK is currently facing is unprecedented [4]. Energy prices jumped 54% in April 2022, the biggest gain since 1970 [5]. Utilising renewable energy instead of fossil fuels for space heating is a potential solution to the current dilemma. Among various renewable energy technologies, solar thermal collection is the most well-developed and common one applied in buildings due to its accessible, sustainable, and clean nature [6]. However, due to the intermittence of solar energy and the mismatch between solar radiation and residential heating demand diurnally and seasonally, it is challenging to fully cover the residential space heating load through the stand-alone solar thermal system [7].

Thermal energy storage (TES) technology is believed to be an effective way of addressing the mismatch between energy supply and demand by converting temporarily available energy into available long-term one [8]. The combination of TES and solar heating allows the thermal energy obtained by the solar collector during the daytime and/or summer to be consumed in the nighttime and/or winter [9]. TES has three common types: sensible thermal energy storage (STES), latent thermal energy storage (LTES) and thermochemical energy storage (TCES) [10]. A TCES system utilises reversible chemical reactions to store thermal energy, which offers a higher energy storage density (ESD, about 200–700 kWh/m^3) compared to the STES and LTES systems [11]. Meanwhile, the TCES system has negligible heat loss during long-term energy storage [6]. These advantages make TCES an appealing strategy for seasonal energy storage in the building sector [12].

The reactant ($A{\bullet}xB$) in the TCES system absorbs heat from a heat source (e.g., solar collector) and decomposes into two products (A and B) in the heat charging phase, during which the heat is converted into stable chemical potential energy and stored in the TCES system. Oppositely, the reverse reaction allows the recombination of the A and B, and

---

[*] Corresponding author.

[**] Corresponding author.

E-mail addresses: mingke.hu@nottingham.ac.uk (M. Hu), yuehong.su@nottingham.ac.uk (Y. Su).

https://doi.org/10.1016/j.renene.2023.02.076
Received 24 November 2022; Received in revised form 25 January 2023; Accepted 17 February 2023

the chemical potential energy is converted back into thermal energy for heating in this stage [13,14]. The reversible chemical reaction of thermochemical materials (TCMs) is described as follows:

$$A\cdot xB_{(solid)} + \Delta H \underset{discharging}{\overset{charging}{\rightleftarrows}} A\cdot(x-y)B_{(solid)} + yB_{(gas)} \tag{1}$$

The relatively low-temperature heat source provided by the typical flat-plate solar thermal collector largely narrows the selection of suitable TCMs for the solar-driven TCES system. Salt hydrates such as $MgCl_2\bullet 6H_2O$ [15], $CaCl_2\bullet 6H_2O$ [16], $SrBr_2\cdot 6H_2O$ [11], and $MgSO_4\bullet 7H_2O$ [17] are widely regarded as the preferred candidate materials in solar-driven TCES systems due to their low regeneration temperatures [17]. For example, $SrBr_2\cdot 6H_2O$ can be utterly dehydrated to stable $SrBr_2\cdot H_2O$ at 80–90 °C [18]. In addition, salt hydrates generally exhibit higher ESD [19]. For instance, $SrBr_2\cdot 6H_2O$ and $MgSO_4\bullet 7H_2O$ are two TCMs with theoretical ESD of over 600 $kWh\bullet m^{-3}$ [20] and nearly 750 $kWh\bullet m^{-3}$ [21], respectively. Besides, salt hydrates commonly react with water vapour or moist air which can be directly discharged into the environment without causing pollution [22]. Fig. 1 depicts the concept of employing a typical salt hydrated-based TCES system for seasonal solar energy storage and building space heating.

However, pure salt hydrates show poor heat and mass transfer properties, which leads to the relatively low thermal efficiency of the TCES system. In addition, agglomerate and swelling of pure salt hydrates due to excessive water vapour absorption results in poor system cycle stability [23]. In order to solve these problems, researchers have developed composite hydrated salt materials containing porous adsorbent (e.g., zeolites [24], expanded vermiculite [25], and expanded graphite [26]) as the host matrix. With high thermal conductivity and porous structure, the host matrixes can effectively improve heat and mass transfer performance of TCMs and avoid agglomeration and expansion, thus enhancing the system thermal efficiency and cycle stability [27]. For example, the thermal conductivity of the composite hydrated salt material composed of expanded natural graphite treated with sulfuric acid (ENG-TSA) and $SrBr_2$ can reach 7.65 $W\bullet m^{-1}\ K^{-1}$, which is about 18 times that of the pure $SrBr_2$ granule salt (i.e., 0.41 $W\bullet m^{-1}\ K^{-1}$) [28]. Meanwhile, ENG-TSA is capable of improving the permeability of the reaction bed from $0.7\bullet 10^{-12}\ m^2$ in the pure state to $2.7\bullet 10^{-12}\ m^2$ in the composite state [29]. Besides, by adding materials such as silica gel can extend the stable cycle number of the $SrBr_2$-based TCES system by four times [30,31]. On the other hand, because the host matrix typically is not involved in the adsorption and desorption processes, the ESD of a composite hydrated salt is generally lower than that of a pure hydrated salt [29]. For example, the theoretical ESD of the $SrBr_2$ -based composite material is around 105 $kWh\bullet m^{-3}$ [32], while the pure $SrBr_2$ exhibited a theoretical ESD of nearly 630 $kWh\bullet m^{-3}$ [19].

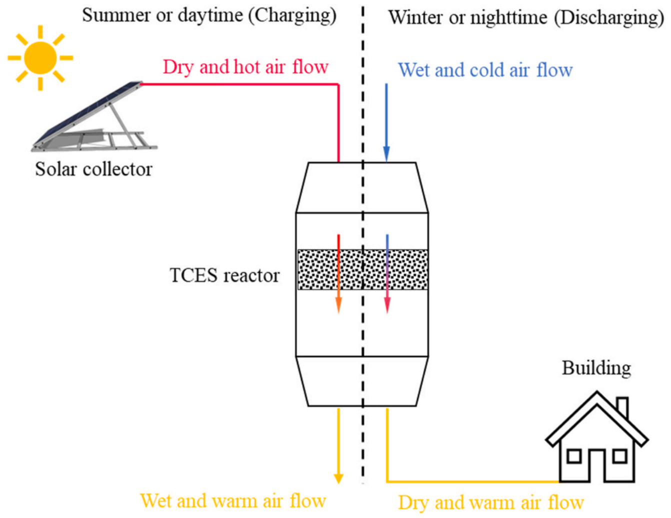

Fig. 1. Schematic diagram of a salt hydrated-based TCES system for energy storage and building space heating.

The structural optimisation of the reaction bed also contributes to the performance enhancement of a TCES system [33]. As long vapour penetration distance in the reaction bed does not favour mass transfer in the salt hydrate-based TCES reactor, and the associated large pressure drop may greatly influence the system efficiency, various novel structures (e.g., honeycomb [34], multi-modular [35] and copper mesh-packed [36] structures) have been proposed and developed to replace the traditional bulk-packed reactor for better permeability [37]. Besides, optimising the operating parameters (e.g. inlet airflow temperature [37], pressure [38] and velocity [39]) can also improve the performance of TCES systems. Aside from the above two points, efforts have also been made from the perspective of system-level optimisation. For example, the TCES system can be integrated with additional components such as the air-source heat pump [36] and solar collector [40] to reduce the external power consumption during the charging process and thus increase the system efficiency.

Basically, the whole family of TCES systems can be divided into two categories: open and closed systems. Considering the superiorities of open systems in terms of system simplicity [41] and efficiency [42], as well as the pollution-free feature of salt hydrates [43], open structures are more common in salt hydrate-based TCES systems. Previous research has shown that, in typical salt hydrate-based open TCES systems, the hot exhaust air during the charging phase is not well-utilised but directly dissipated to the ambient. If this exhaust heat can be partly recovered to pre-heat the inlet ambient air, the performance of the TCES system can be enhanced. Therefore, a solar PV/T-powered TCES system integrating a heat exchanger (PV/T-TCES-HEX system) is proposed in the present work to demonstrate the benefit resulting from this heat recovery scheme. Given that existing simulation studies on TCES systems basically focused only on steady-state performance analyses which cannot fully reveal the behaviour of the system in real-world applications, especially for those solar-driven TCES systems operating in dynamic weather conditions (e.g., solar irradiance, ambient air temperature, wind velocity), this study developed a dynamic model based on COMSOL to evaluate the charging performance of the PV/T-TCES-HEX system under actual ambient conditions. Parametric sensitive analyses were also conducted to investigate the effect of some critical operational and structural parameters (e.g., air mass flow rate, reaction bed thickness and length) on the charging performance of the proposed system.

2. System description

Fig. 2 presents the schematic diagram of the charging process of the proposed PV/T-TCES-HEX system in the charging process. The system mainly consists of a TCES reaction bed, an air-to-air heat exchanger (HEX), an air-based PV/T collector, an auxiliary electric heater, and an air blower. During the charging process, the low-temperature ambient air flows into the HEX and is preheated by the hot exhaust air from the TCES reactor. Then, the preheated air enters into the PV/T collector and extracts heat from the PV/T absorber for further air-temperature upgrading and PV efficiency enhancement. The auxiliary heater powered by electricity from the PV/T collector and/or external power grid is used in case the air temperature at the outlet of the PV/T collector is below the set point (e.g., 90 °C). After that, the high-temperature air is blown into the TCES reactor to provide heat for the dehydration of the salt hydrate. After the dehydration process, the airstream leaving the reactor is still at a high temperature. Therefore, the airstream is routed to the HEX for heat recovery before eventually being exhausted to the ambient.

Fig. 3 shows the 3D structure of the combined TCES reactor and HEX unit. The square pipe on the right side of the model is the inlet of the reactor, and the left side of the reactor is directly connected to the HEX. The reactor is composed of eight reaction beds, and each reaction bed

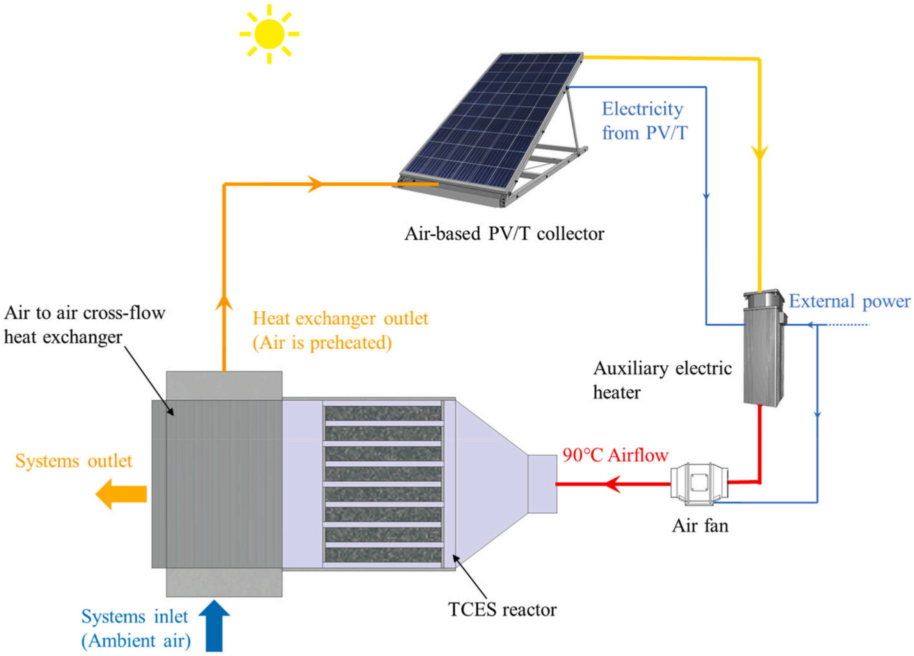

Fig. 2. Schematic diagram of the PV/T-TCES-HEX system working in the charging process.

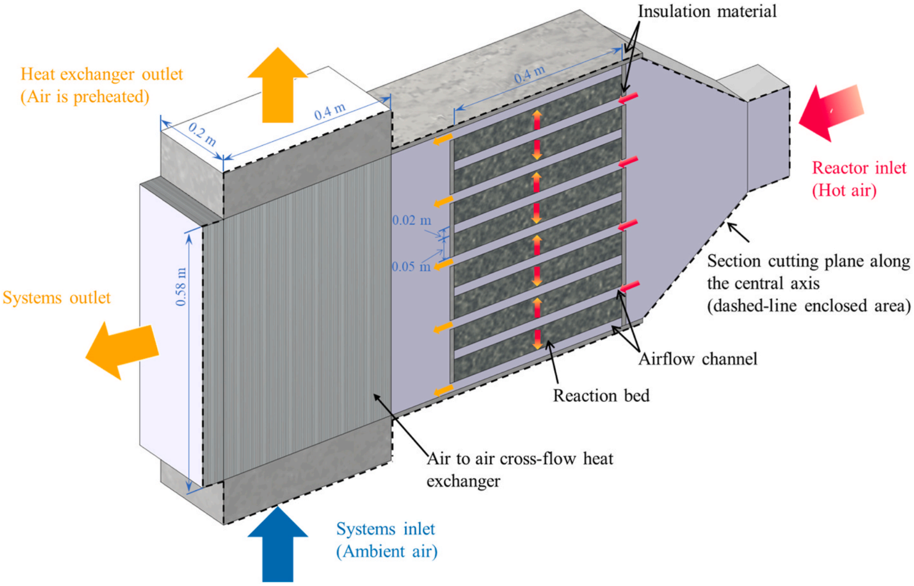

Fig. 3. 3D schematic diagram of the combined TCES reactor and HEX unit with a section cutting plane along the central axis.

has a dimension of 400 mm × 400 mm × 50 mm (length × width × heigh). The intervals of the reaction beds constitute four air inlet channels and five air outlet channels, each with a height of 20 mm and these channel ends are closed. Hot air flows into the inlet channel and then is forced to flow through the reactor bed (up or down) into the outlet channel. Finally, it leaves the reactor and flows into the HEX for heat recovery. The external surface of the combined TCES reactor and HEX unit is surrounded by a thermal insulation layer to minimise heat loss during the charging and discharging processes. This novel design allows the reactor to realize a better heat and mass transfer performance. Water vapour generated during the charging process could be evacuated quickly, and thus a relatively high conversion rate can be assured. In addition, the layered structure also avoids deliquescence or agglomeration of granular salts due to excessive water vapour absorption during the discharging period. Compared with the traditional TCES reactor, this design incorporates a HEX, allowing better utilisation of the thermal energy collected by the PV/T collector and increasing the overall thermal efficiency of the TCES system. The reaction bed consists of metal trays holding vermiculite impregnated with 43 wt% $CaCl_2$ as the TCM. The reversible chemical reaction of $CaCl_2$ is described below [44]:

$$CaCl_2 \cdot 6H_2O_{(solid)} + \Delta H \underset{\text{Discharging}}{\overset{\text{Charging}}{\rightleftarrows}} CaCl_{2(solid)} + 6H_2O_{(gas)} \tag{2}$$

The structure of the air-based PV/T collector is shown in Fig. 4. It consists of a glass cover, PV cells, an aluminium substrate, an airflow channel, and a thermal insulation layer. The length and width of the effective irradiation-collection surface of the collector are 1.964 m and 0.964 m, respectively. 72 pieces of monocrystalline silicon PV cells with a total area of 1.12 m^2 are packaged and attached to the aluminium substrate, and the rest area of the aluminium substrate is covered with

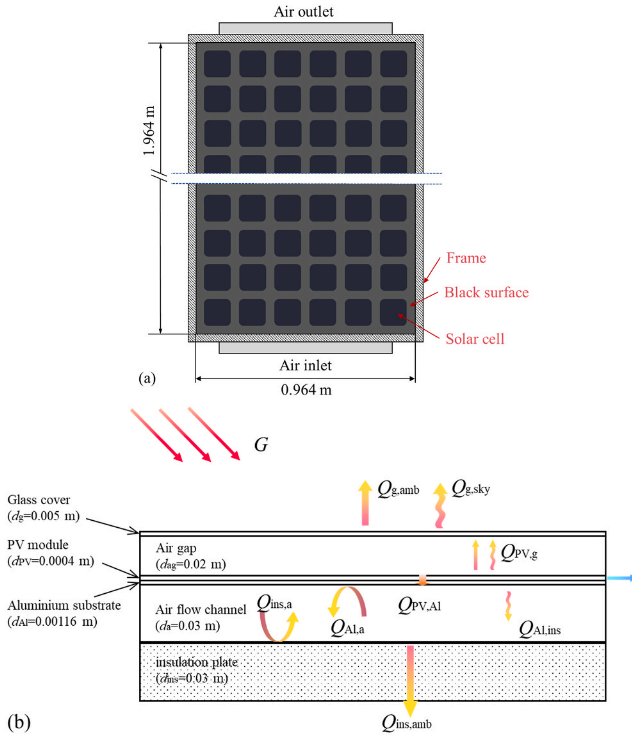

Fig. 4. Schematic diagram of the air-based PV/T collector: (a) Top view; (b) Cross-section view with electricity and heat transfer illustration.

black Tedlar–polyester–Tedlar (TPT). The glass cover is arranged on top of the PV/T plate with an 0.02 m air gap to reduce convective heat loss. Below the aluminium substrate is an airflow channel with a height of 0.03 m. A 0.03 m-thick glass fibre is employed as the thermal insulation layer to suppress the backside thermal loss of the PV/T collector. The solar collector is mounted at an inclination angle of 53° facing due south to obtain the maximum annual solar irradiance on the assumption that the PV/T-TCES-HEX system is located in Nottingham, UK (53°N, 1°W).

3. Mathematical model

To quantitatively assess the charging performance of the proposed PV/T-TCES-HEX system, a mathematical model is developed, including the sub-model for the TCES reactor and the PV/T collector, respectively. This numerical study adopts some assumptions to establish the governing equations describing the mass and energy transfers in the TCES reactor and PV/T collector.

1. The reaction bed has a local thermal equilibrium between the TCMs and airflow [38,45,46].
2. Radiative heat transfer in the combined TCES reactor and HEX unit and heat loss through the frame of the PV/T collector is neglected [45–47].
3. The airflow in this study is regarded as an ideal gas, and it is uniform and follows the Darcy's law in the reaction bed [38,46].
4. The TCM is uniformly distributed in the reaction bed. Furthermore, the effect of the sieve plate at the bottom of the reaction bed on the solid-gas reaction is ignored [37].
5. The thermophysical properties of the reaction bed, TCMs and PV/T collector are constant [37,48].
6. All components in the PV/T-TCES-HEX system have an equal initial temperature.

3.1. Mathematical model for the TCES reactor

According to the assumptions listed above, the mass transfer and heat balance equations for the TCES reactor are described below.

3.1.1. Reaction kinetics

The reaction kinetics of salt hydrate can be defined in terms of three main variables: time-dependent conversion degree X, pressure P, and temperature T [49]. The conversion rate of salt hydrate in the charging process is expressed as:

$$\frac{\partial X}{\partial t}=R_{\mathrm{kin}}(1-X)\left(1-\frac{P_{\mathrm{v}}}{P_{\mathrm{eq}}}\right)=A_{\mathrm{freq}}\exp\left(-\frac{E_{\mathrm{a}}}{RT}\right)(1-X)\left(1-\frac{P_{\mathrm{v}}}{P_{\mathrm{eq}}}\right) \tag{3}$$

where X is the conversion degree; R_{kin} is the chemical kinetic factor, s^{-1}; P_{v} and P_{eq} are the partial pressure and equilibrium pressure of water vapour in the reactor, respectively, Pa; A_{freq} is the pre-exponential Arrhenius factor, s^{-1}; R is the ideal gas constant $J{\bullet}mol^{-1}{\bullet}K^{-1}$, and E_{a} refers to the Arrhenius activation energy, $J{\bullet}mol^{-1}$.

The conversion degree of the salt hydrate can be defined as:

$$X(t)=\frac{c_{\mathrm{s,i}}-c_{\mathrm{s}}(t)}{c_{\mathrm{s,i}}-c_{\mathrm{s,f}}} \tag{4}$$

where $c_{\mathrm{s,i}}$ and $c_{\mathrm{s,f}}$ are respectively the initial and final molar concentration of the salt hydrate ($CaCl_2{\bullet}6H_2O$) in the reaction bed, $mol{\bullet}m^{-3}$.

Assuming that during the solid-gas reaction process, the mass transfer and chemical reaction process are fast enough to keep the whole process at prevailing temperature, the equilibrium pressure P_{eq} and temperature T can be related by the Clausius-Clapeyron equation and is calculated by:

$$\ln\left(\frac{P_{\mathrm{eq}}}{P_{\mathrm{ref}}}\right)=-\frac{\Delta H_{\mathrm{r}}}{RT_{\mathrm{ref}}}+\frac{\Delta S_{\mathrm{r}}}{R} \tag{5}$$

where P_{ref} is the reference pressure, Pa; ΔH_{r} is the reaction enthalpy, $kJ{\bullet}mol^{-1}$; T_{ref} is the reference temperature, K; and ΔS_{r} is the reaction entropy, $J{\bullet}mol^{-1}{\bullet}K^{-1}$.

3.1.2. Mass conservation

Assuming there is no mass exchange between the reactor and external environment, the density of the hydrated salt decreases with the charging process, and the density of the dehydrated salt and water vapour increases. The mass transfer equation for the water vapour can be defined as:

$$\delta\frac{\partial\rho_{\mathrm{v}}}{\partial t}=S_{\mathrm{w}}-\nabla(\rho_{\mathrm{v}}\vec{u})+D_{\mathrm{g}}\Delta\rho_{\mathrm{v}} \tag{6}$$

where δ is the porosity of the salt hydrate composite material and is set at 0.64 [50]; ρ_{v} is the density of water vapour, $kg{\bullet}m^{-3}$; $\vec{u}$ is the velocity vector, $m{\bullet}s^{-1}$; D_{g} is the diffusion coefficient of water vapour in the reaction bed, $m^2{\bullet}s^{-1}$; and S_{w} is the mass source and is expressed as:

$$S_{\mathrm{w}}=zc_{\mathrm{s,i}}\frac{\partial X}{\partial t}M_{\mathrm{v}} \tag{7}$$

where z is the stoichiometric number of the reaction; and M_{v} is the molecular mass of water vapour, $g{\bullet}mol^{-1}$.

Besides, the density of the moist air mixture (ρ_{m}) can be calculated by:

$$\frac{\partial(\delta\rho_{\mathrm{m}})}{\partial t}+\nabla(\rho_{\mathrm{m}}\vec{u})=S_{\mathrm{w}} \tag{8}$$

3.1.3. Mass transport

The moist air passing through the reaction bed conforms to the Brinkman–Forchheimer extended Darcy model, and the mass transport equation is expressed as:

$$\frac{\partial}{\partial t}(\rho_{\mathrm{m}}\vec{u}) + \left(\frac{\vec{u}}{\delta}\nabla\right)(\rho_{\mathrm{m}}\vec{u}) = \nabla\left[-\delta\overrightarrow{P_{\mathrm{v}}}\mathrm{I} + \mu(\nabla\vec{u} + (\nabla\vec{u})^{T} - \frac{2}{3}\mu\left(\vec{u}\right)\mathrm{I})\right] + S_{\mathrm{w}}\frac{\vec{u}}{\delta} - \delta\frac{\mu}{\varphi}\vec{u} \tag{9}$$

where φ is the permeability of the hydrate composite in the reaction bed, m^2; and μ is the dynamic viscosity of the moist air mixture, Pa•s.

3.1.4. *Energy conservation*

The energy balance equation in the TCES reactor is described as:

$$(1-\delta)\rho_{\mathrm{s}}C_{\mathrm{s}}\frac{\partial T}{\partial t} = \nabla\left(k_{\mathrm{eff}}\nabla T\right) - C_{\mathrm{v}}\rho_{\mathrm{v}}\vec{u}\nabla T + \dot{q} \tag{10}$$

where ρ_{s} is the density of the salt hydrate, kg•m^{-3}; C_{s} and C_{v} are the specific heat of the salt hydrate and water vapour, J•kg^{-1}•K^{-1}; k_{eff} is the effective thermal conductivity of the reaction bed, W•m^{-1}•K^{-1}; and $\dot{q}$ is the heat absorbed by the salt hydrate in the charging process, W•m^{-3}.

The effective thermal conductivity of the reaction bed can be expressed as follows:

$$k_{\mathrm{eff}} = (1-\delta)k_{\mathrm{s}} + \delta k_{\mathrm{v}} \tag{11}$$

where k_{s} and k_{v} represent the thermal conductivity of the solid salt and water vapour, respectively, W•m^{-1}•K^{-1}.

The heat absorbed by the salt hydrate is described as:

$$\dot{q} = \pm z c_{\mathrm{s,i}}\frac{\partial X}{\partial t}\Delta H_{\mathrm{r}} \tag{12}$$

As the TCES reactor is typically placed in an indoor environment where the local wind speed is nearly zero, only natural convective heat exchange occurs between the TCES reactor and its surroundings. Therefore, the heat balance equation on the external surface of the TCES reactor is described as:

$$-\mathbf{n}(k_{\mathrm{ins}}\nabla T_{\mathrm{ins}}) = h_{\mathrm{ins,ind}}(T_{\mathrm{ind}} - T_{\mathrm{ins}}) \tag{13}$$

where k_{ins} is the thermal conductivity of the insulating material, W•m^{-1}•K^{-1}; $h_{\mathrm{ins,ind}}$ is the natural convective heat transfer coefficient between the reactor and indoor air and is determined by COMSOL in this study, W•m^{-2}•K^{-1}); T_{ind} is the indoor air temperature, K.

Table 1 lists some key parameters of the TCES reactor and their respective values used in this simulation study.

3.2. *Mathematical model for the PV/T collector*

The energy flow process of the PV/T collector is shown in Fig. 4. Accordingly, the energy balance equation for each part in the PV/T collector (i.e., glass cover, PV module, aluminium substrate, airflow in the air channel and insulation plate) is established.

Table 1

Key parameters of the TCES reactor.

Parameters	Description	Value
M_{v}	Molecular mass of water vapour (g•mol^{-1})	18.02
M_{s}	Molecular mass of salt hydrate (g•mol^{-1})	219.08
$c_{\mathrm{s,i}}$	Molar concentration (mol•m^{-3})	609
φ	Permeability of salt hydrate (m^2)	2.7•10^{-12}
$T_{\mathrm{in,r}}$	Airflow temperature at reactor inlet (°C)	90
P_{ref}	Reference pressure (Pa)	101,325
D_{g}	Gas diffusion coefficient (m^2•s^{-1})	2.82·10^{-5}
Δ	Porosity	0.64
E_{a}	Activation energy ((J•mol^{-1})	5.5•10^4
R	Ideal gas constant (J•mol^{-1}•K^{-1})	8.134
ΔH_{r}	Reaction enthalpy (kJ•mol^{-1})	53.4
k_{ins}	Thermal conductivity of the insulating material (W•m^{-1}•K^{-1})	0.0035
L	Length of the reaction bed (m)	0.4
W	Width of the reaction bed (m)	0.4
H	Heigh of the reaction bed (m)	0.05
d_{r}	Heigh of the airflow channel (m)	0.02

3.2.1. *Energy balance equation for the glass cover*

The energy balance equation for the glass cover is described as:

$$\rho_{\mathrm{g}}C_{\mathrm{g}}\frac{\partial T_{\mathrm{g}}}{\partial t} = k_{\mathrm{g}}\nabla^2 T_{\mathrm{g}} + h_{\mathrm{amb,g}}\left(T_{\mathrm{amb}} - T_{\mathrm{g}}\right) + h_{\mathrm{sky,g}}\left(T_{\mathrm{sky}} - T_{\mathrm{g}}\right) + h_{\mathrm{PV,g}}\left(T_{\mathrm{PV}} - T_{\mathrm{g}}\right) + G\alpha_{\mathrm{g}} \tag{14}$$

where ρ_{g}, C_{g}, and k_{g} are the density, specific heat capacity, and thermal conductivity of the glass cover, kg•m^{-3}, J•kg^{-1}•K^{-1} and W•m^{-1}•K^{-1}), respectively; T_{g}, T_{amb}, T_{sky}, and T_{PV} are the temperature of the cover, ambient air, sky, and PV module, respectively, K; $h_{\mathrm{amb,g}}$ is the convective heat transfer coefficient between the glass cover and ambient, W•m^{-2}·K^{-1}; $h_{\mathrm{sky,g}}$ refers to the radiative heat transfer coefficient between the glass cover and sky, W•m^{-2}·K^{-1}; $h_{\mathrm{PV,g}}$ is the overall heat transfer coefficient between the glass cover and PV module, W•m^{-2}·K^{-1}. α_{g} is the solar absorptivity of the glass cover; and G is the solar irradiance, W•m^{-2}.

The convective heat transfer coefficient between the glass cover and PV module can be described as [51]:

$$h_{\mathrm{amb,g}} = 2.8 + 3.0u_{\mathrm{w}} \tag{15}$$

where u_{w} is the ambient wind speed, m•s^{-1}.

The radiative heat transfer coefficient between the glass cover and PV module is shown as follows [52]:

$$h_{\mathrm{sky,g}} = \varepsilon_{\mathrm{g}}\sigma\left(T_{\mathrm{sky}}^2 - T_{\mathrm{g}}^2\right)\left(T_{\mathrm{sky}} + T_{\mathrm{g}}\right) \tag{16}$$

where ε_{g} is the emissivity of the glass cover; σ is the Stefan–Boltzmann constant; and T_{sky} is the sky temperature and can be calculated by Ref. [47]:

$$T_{\mathrm{sky}} = 0.00552T_{\mathrm{amb}}^{1.5} \tag{17}$$

In this model, the emissivity of the PV module and black surface is set to be equal, and thus the heat transfer coefficient between the glass cover and PV module can be described as [53]:

$$h_{\mathrm{PV,g}} = \sigma\left(T_{\mathrm{PV}}^2 + T_{\mathrm{g}}^2\right)\left(T_{\mathrm{PV}} + T_{\mathrm{g}}\right)\left(\frac{1}{1/\varepsilon_{\mathrm{PV}} + 1/\varepsilon_{\mathrm{g}} - 1}\right) + Nu\frac{k_{\mathrm{a}}}{d_{\mathrm{ag}}} \tag{18}$$

where Nu is the Nusselt number; k_{a} is the thermal conductivity of air, W•m^{-1}·K^{-1}; and d_{ag} is the air gap height between the glass cover and PV module, m.

For collectors with inclinations from 0° to 75°, the Nusselt number can be obtained by Ref. [54]:

$$Nu = 1 + 1.44\left(1 - \frac{1708(\sin 1.8\,\beta)^{1.6}}{Ra\cdot\cos\beta}\right)\left[1 - \frac{1078}{Ra\cdot\cos\beta}\right]^{+} + \left[\left(\frac{Ra\cdot\cos\beta}{5380}\right)^{1/3} - 1\right]^{+} \tag{19}$$

where β is the inclination angle of the solar collector; and Ra is the Rayleigh number. The + indicates that only positive values are adopted for the terms within square brackets; in the case of negative, the term adopts zero.

3.2.2. *Energy balance equation for the PV module*

The energy balance equation for the PV module is expressed as:

$$\rho_{\mathrm{PV}}C_{\mathrm{PV}}\frac{\partial T_{\mathrm{PV}}}{\partial t} + \xi E_{\mathrm{PV}} = k_{\mathrm{PV}}\nabla^2 T_{\mathrm{PV}} + h_{\mathrm{PV,g}}\left(T_{\mathrm{PV}} - T_{\mathrm{g}}\right) + \frac{(T_{\mathrm{Al}} - T_{\mathrm{PV}})}{R_{th}} + G(\tau\alpha)_{\mathrm{PV}} \tag{20}$$

where ρ_{PV}, C_{PV}, and k_{PV} are the density, specific heat capacity, and thermal conductivity of the PV module, kg•m^{-1}, J•kg^{-1}•K^{-1}, and W•m^{-1}•K^{-1}, respectively; T_{Al} is the temperature of the aluminium substrate, K; ξ is the packing factor of the PV module; E_{PV} is the output electrical power of the PV module, W•m^{-2}; R_{th} is the thermal resistance of the adhesive layer between the PV module and the aluminium substrate, m^2·K•W^{-1}; and $(\tau\alpha)_{\mathrm{PV}}$ is the effective transmissivity–absorptivity product of the PV module and is expressed as [52]:

$$(\tau\alpha)_{\mathrm{PV}} = \frac{\tau_{\mathrm{g}}\alpha_{\mathrm{PV}}}{1-(1-\alpha_{\mathrm{PV}})\rho_{\mathrm{g}}} \tag{21}$$

where α_{PV} is the absorptivity of the PV module; τ_{g} is the transmissivity of the glass cover; and ρ_{g} is the reflectivity of the glass cover.

The output electrical power of the PV module is expressed as [55]:

$$E_{\mathrm{PV}} = G\tau_{\mathrm{g}}\eta_{\mathrm{ref}}\left[1-B_{\mathrm{r}}\left(T_{\mathrm{PV}}-T_{\mathrm{ref}}\right)\right] \tag{22}$$

where η_{ref} is the reference efficiency of the PV module at T_{ref} (25 °C); and B_{r} is the temperature coefficient of the PV module.

3.2.3. Energy balance equation for the aluminium substrate

The energy balance equation for the aluminium substrate is written as:

$$\rho_{\mathrm{Al}}C_{\mathrm{Al}}\frac{\partial T_{\mathrm{Al}}}{\partial t} = k_{\mathrm{Al}}\nabla^2 T_{\mathrm{Al}} + \frac{(T_{\mathrm{PV}}-T_{\mathrm{Al}})}{R_{th}} + h_{\mathrm{Al,a}}(T_{\mathrm{a}}-T_{\mathrm{Al}}) + h_{\mathrm{Al,ins}}(T_{\mathrm{ins}}-T_{\mathrm{Al}}) \tag{23}$$

where ρ_{Al}, C_{Al}, and k_{Al} are the density, specific heat capacity, and thermal conductivity of the aluminium substrate, kg•m^{-1}, J•kg^{-1}•K^{-1}, and W•m^{-1}•K^{-1}, respectively; T_{a} and T_{ins} are the temperature of the air and insulation plate, K; $h_{\mathrm{Al,a}}$ is the convective heat transfer coefficient between the aluminium substrate and airflow, W•m^{-2}·K^{-1}; and $h_{\mathrm{Al,ins}}$ is the radiative heat transfer coefficient between the aluminium substrate and insulation plate, W•m^{-2}·K^{-1}.

The convective heat transfer coefficient between the aluminium substrate and airflow is described as [54]:

$$h_{\mathrm{Al,a}} = Nu\frac{k_{\mathrm{a}}}{d_{\mathrm{Al,ins}}} = 0.023Re^{0.8}Pr^{0.4}\frac{k_{\mathrm{a}}}{d_{\mathrm{Al,ins}}} \tag{24}$$

where $d_{\mathrm{Al,ins}}$ is the height of the air channel, m; Re is the Reynolds number; and Pr is the Prandtl number.

The heat transfer coefficient between the aluminium substrate and insulation plate is derived by Ref. [52]:

$$h_{\mathrm{Al,ins}} = \sigma\left(T_{\mathrm{Al}}^2+T_{\mathrm{ins}}^2\right)(T_{\mathrm{Al}}+T_{\mathrm{ins}})\left(\frac{1}{1/\varepsilon_{\mathrm{Al}}+1/\varepsilon_{\mathrm{ins}}-1}\right) \tag{25}$$

where $\varepsilon_{\mathrm{Al}}$ and $\varepsilon_{\mathrm{ins}}$ are the emissivity values of the aluminium substrate and insulation plate, respectively.

3.2.4. Energy balance equation for the airflow in the air channel

The energy balance equation for the airflow in the air channel is described as:

$$\rho_{\mathrm{a}}C_{\mathrm{a}}\frac{\partial T_{\mathrm{a}}}{\partial t} + \rho_{\mathrm{a}}C_{p,\mathrm{a}}\vec{u}\nabla T_{\mathrm{a}} = k_{\mathrm{a}}\nabla^2 T_{\mathrm{a}} + h_{\mathrm{Al,a}}(T_{\mathrm{Al}}-T_{\mathrm{a}}) + h_{\mathrm{ins,a}}(T_{\mathrm{ins}}-T_{\mathrm{a}}) \tag{26}$$

where ρ_{a}, C_{a}, and k_{a} are the density, specific heat capacity, and thermal conductivity of the airflow, kg•m^{-1}, J•kg^{-1}•K^{-1}, and W•m^{-1}•K^{-1}, respectively; $h_{\mathrm{ins,a}}$ is the convective heat transfer coefficients between the airflow and insulation plate, and it is the same as $h_{\mathrm{Al,a}}$ in expression.

3.2.5. Energy balance equation for the insulation plate

The energy balance equation for the insulation plate is written as:

$$\rho_{\mathrm{ins}}C_{\mathrm{ins}}\frac{\partial T_{\mathrm{ins}}}{\partial t} = k_{\mathrm{ins}}\nabla^2 T_{\mathrm{ins}} + h_{\mathrm{ins,a}}(T_{\mathrm{ins}}-T_{\mathrm{a}}) + h_{\mathrm{Al,ins}}\left(T_{\mathrm{ins}}-T_{\mathrm{ap}}\right) + U_{\mathrm{ins,amb}}(T_{\mathrm{amb}}-T_{\mathrm{ins}}) \tag{27}$$

where ρ_{ins}, C_{ins}, and k_{ins} are the density, specific heat capacity, and thermal conductivity of the insulation plate, kg•m^{-1}, J•kg^{-1}•K^{-1}, and W•m^{-1}•K^{-1}; and $U_{\mathrm{ins,amb}}$ is the overall heat transfer coefficient between the insulation plate and ambient and can be calculated by Ref. [52]:

$$U_{\mathrm{ins,amb}} = \frac{1}{\left(\frac{1}{h_{\mathrm{ins,amb}}}+\frac{d_{\mathrm{ins}}}{k_{\mathrm{ins}}}\right)} \tag{28}$$

where $h_{\mathrm{ins,amb}}$ is the convective heat transfer coefficient between the insulation plate and ambient air, and it is the same as $h_{\mathrm{amb,g}}$ in expression.

The design parameters of the PV/T collector and their respective values used in this simulation study are listed in Table 2.

3.3. Performance evaluation metrics

The power assurance rate of the PV/T collector to the PV/T-TCES-HEX system is defined as:

$$PAR_{\mathrm{PV/T}} = \frac{W_{\mathrm{PV/T}}}{W_{\mathrm{sys}}} = \frac{W_{\mathrm{PV/T}}}{W_{\mathrm{PV/T}}+W_{\mathrm{e}}} \tag{29}$$

where $W_{\mathrm{PV/T}}$ is the energy from the PV/T collector, kWh; W_{sys} is the total energy consumption of the system, kWh; and W_{e} is the external electricity consumption (excluding the electricity provided by the PV/T collector), kWh.

The energy from the PV/T collector ($W_{\mathrm{PV/T}}$) can be expressed as:

$$W_{\mathrm{PV/T}} = \int\left[\dot{m}C_{\mathrm{a}}\left(T_{\mathrm{out,c}}-T_{\mathrm{in,c}}\right)+E_{\mathrm{PV}}\right]dt \tag{30}$$

where $\dot{m}$ is the mass flow rate of the airflow, kg•s^{-1}; $T_{\mathrm{in,c}}$ and $T_{\mathrm{out,c}}$ are the airflow temperature at the inlet and outlet of the solar collector, respectively, K.

The external electricity consumption can be expressed as:

$$W_{\mathrm{e}} = W_{\mathrm{h}} + W_{\mathrm{fan}} \tag{33}$$

where W_{h} is the external electricity consumed by the heater, kWh; and

Table 2
Design parameters of the PV/T collector.

Component	Parameters	Value
Glass cover	Area (m^2)	1.89
	Solar absorptivity	0.038
	Emissivity	0.88
	Solar transmissivity	0.912
	Thermal conductivity, W•m^{-1}•K^{-1}	0.038
	Specific heat capacity, J•kg^{-1}•K^{-1}	750
	Density, kg•m^{-3}	2203
PV module	Solar absorptivity	0.9
	Emissivity	0.95
	Packing factor	0.59
	Thermal conductivity, W•m^{-1}•K^{-1}	149
	Specific heat capacity, J•kg^{-1}•K^{-1}	700
	Density, kg•m^{-3}	600
	Reference efficiency	0.135
	Temperature coefficient, K^{-1}	0.0045
Aluminium substrate	Emissivity	0.1
	Thermal conductivity, W•m^{-1}•K^{-1}	237
	Specific heat capacity, J•kg^{-1}•K^{-1}	903
	Density, kg•m^{-3}	2700
Insulation plate	Emissivity	0.2
	Thermal conductivity, W•m^{-1}•K^{-1}	0.046
	Specific heat capacity, J•kg^{-1}•K^{-1}	670
	Density, kg•m-3	30

W_{fan} is the external electricity consumed by the air fan, kWh.

The external electricity consumed by the heater can be expressed as:

$$W_{\text{h}} = \frac{\int \left[\dot{m} C_{\text{a}} \left(T_{\text{in,r}} - T_{\text{out,c}} \right) - \eta_{\text{h}} E_{\text{PV}} \right] \text{d}t}{\eta_{\text{h}}} \tag{34}$$

where $T_{\text{in,r}}$ is the airflow temperature at the inlet of the reactor, K; η_h is the auxiliary heater efficiency and is set at 0.9.

The external electricity consumed by the air fan can be calculated by:

$$W_{\text{fan}} = \frac{\int (\Delta P \dot{\gamma}) \text{d}t}{\eta_{\text{fan}}} \tag{35}$$

where ΔP is the differential pressure between the system inlet and outlet, Pa; $\dot{\gamma}$ is the volume flow rate of air, $m^3 \bullet s^{-1}$; and η_{fan} is the fan efficiency [56].

The thermal efficiency of the proposed system in the charging process is defined as:

$$\eta_{\text{E}} = \frac{Q_{\text{ch}}}{W_{\text{e}}} \tag{32}$$

The stored heat of the system in the charging process (Q_{ch}) can be expressed as:

$$Q_{\text{ch}} = \int \dot{m} C_{\text{a}} \left(T_{\text{in,r}} - T_{\text{out,r}} \right) \text{d}t \tag{31}$$

where $T_{\text{out,r}}$ is the airflow temperature at the outlet of the reactor, K.

4. Model validation

The equations, initial and boundary conditions are coupled and solved by the finite element analysis software COMSOL Multiphysics 5.6, and the fine mesh is selected after grid independence analysis. The established mathematical model is validated by comparing it with the experimental data reported in the literature, including an experimental study of an open TCES system using vermiculite- $CaCl_2 \bullet 6H_2O$ as the TCM [44] and an experimental investigation of a tri-functional PV/T collector working in air-heating mode [57]. The *RMSD* (root mean square deviation) of some key parameters is evaluated via Eq. (34) [58]:

$$RMSD = \sqrt{\frac{\sum \left[\left(x_{\text{sim,i}} - x_{\text{exp,i}} \right) / x_{\text{exp,i}} \right]^2}{n}} \tag{36}$$

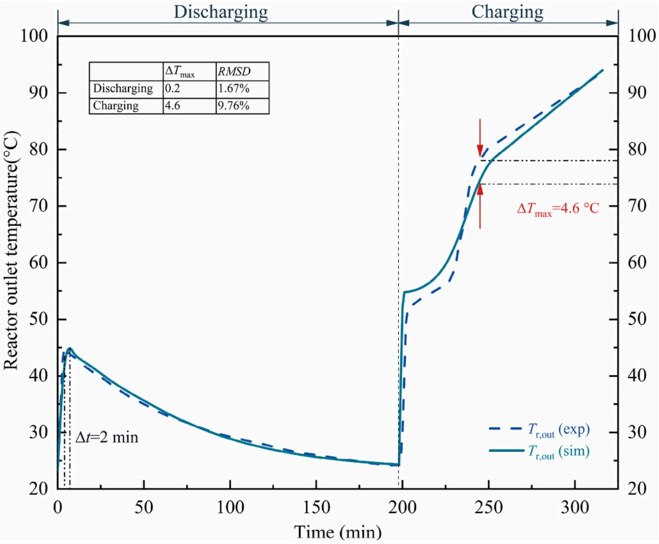

Fig. 5. Simulation and experiment results of vermiculite-$CaCl_2$ cyclic testing [50].

The temperature curve of the reactor bed obtained by the simulation and experiment are compared in Fig. 5. The first stage is the discharge process, in which the simulated and measured bed temperatures reach the highest at the 7th and 9th minute, respectively. The maximum temperature difference is only 0.2 °C. The second stage is the charging process, during which the bed temperature difference between the experiment and simulation peaks at 4.6 °C and is less than 1 °C at the end. The *RMSD* of the bed temperature in the discharging and charging phases are 1.67% and 9.76%, respectively. Regarding the validation of the sub-model for the PV/T collector, the simulated and experimental results of the airflow temperature at the outlet of the PV/T collector, the PV module temperature and the electrical output power are shown in Fig. 6. The *RMSD* of these three parameters is 2.28%, 4.67% and 13.61%, respectively. The comparison indicates that the simulation results using the above mathematical model are in good agreement with the experimental data. Therefore, the mathematical model developed in Section 3 is valid in predicting the performance of the proposed PV/T-TCES-HEX system.

5. Results and discussion

Based on the mathematical modelling, the thermal performance of the PV/T-TCES-HEX system in the charging process is numerically analyzed and compared with a stand-alone TCES system (hereafter referred to as the “TCES-only system”) and a hybrid TCES and HEX system (hereafter referred to as the “TCES-HEX system”). In addition, the effect of some key parameters on the charging performance of the PV/T-TCES-HEX system is evaluated.

5.1. *Full-day charging performance of the PV/T-TCES-HEX system*

The full-day charging performance of the PV/T-TCES-HEX system is investigated firstly. The typical meteorological year data on 17th June for Nottingham, UK are employed from Climate.OneBuild.Org [59] (as seen in Fig. 7). The average solar radiation in the studied period (i.e., from 06:00 to 18:00) is 556.58 $W \bullet m^{-2}$, and the average ambient temperature, relative humidity level, and wind velocity are 16.28 °C, 58.61% and 1.17 $m \bullet s^{-1}$, respectively. The airflow temperature at the system inlet is equal to the ambient temperature in this case study, and the mass flow rate of the airflow is 0.03 $kg \bullet s^{-1}$. During the whole charging process, the airflow is constantly heated up to 90 °C before entering into the TCES reactor. The airflow temperatures at the outlet of the TCES reactor ($T_{\text{r,out}}$), the outlet of the HEX (PV/T side, $T_{\text{HEX,out}}$), and

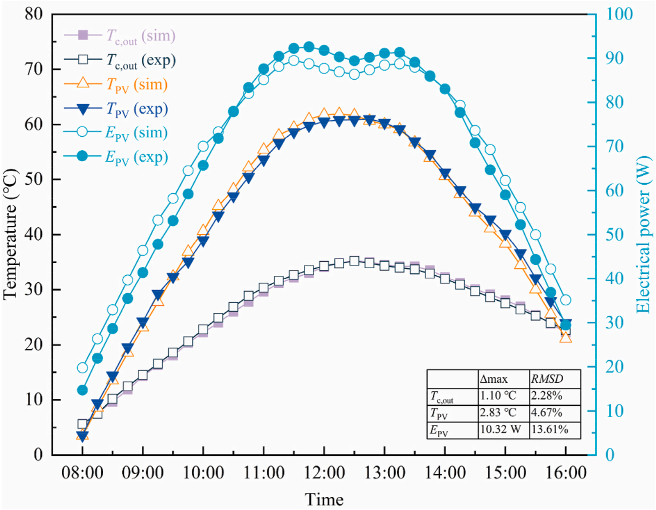

Fig. 6. Simulated outlet air temperature, PV module temperature and electrical output compared with the experimental measurements [57].

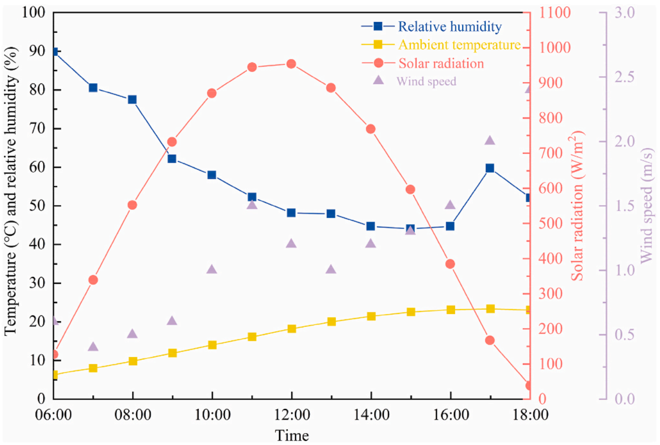

Fig. 7. Typical meteorological year data on 17th June for Nottingham, UK [59].

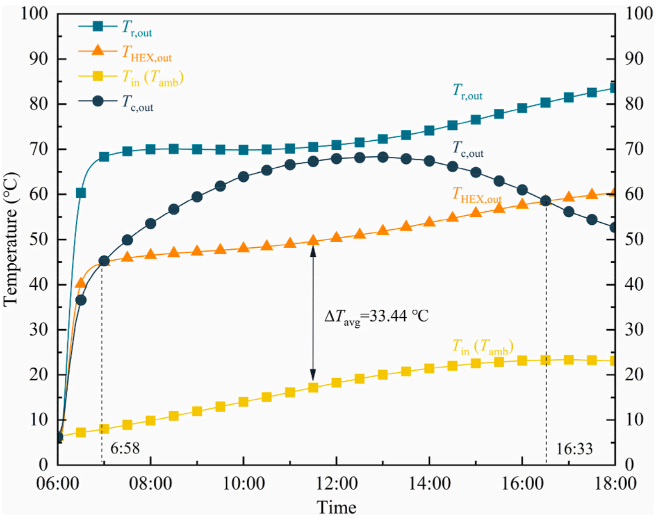

Fig. 8. Airflow temperatures at the outlet of the TCES reactor, HEX (PV/T side), and PV/T collector in the PV/T-TCES-HEX system.

the outlet of the PV/T collector ($T_{c,out}$) during the charging process are depicted in Fig. 8, and the temperature distributions of the combined TCES reactor and HEX unit (including that of the section cutting plane along the central axis) and the PV/T collector at 7:00, 12:00 and 15:00 are shown in Fig. 9. In the very beginning (unsteady state), the $T_{r,out}$ shows a sharp rise until it reaches around 70 °C. After that, the $T_{r,out}$ reaches a plateau until around 12:00, indicating that the TCES reactor operates in a quasi-steady state with a relatively stable conversion rate during this period. At the next stage, the $T_{r,out}$ experiences a gradual increase till the end, suggesting a gradual decrease in the conversion rate. The $T_{HEX,out}$ is affected by both the T_{in} and $T_{r,out}$ but mainly follows the variation trend of the $T_{r,out}$ due to the significant fluctuation of the latter. Besides, an average temperature difference of 33.44 °C between the $T_{HEX,out}$ and T_{in} signifies the effective heat recovery attributed to the integration of the HEX. The variation of the $T_{c,out}$ is generally in line with the solar irradiance curve. The $T_{c,out}$ is lower than the $T_{HEX,out}$ before 6:58 and after 16:33, indicating that the PV/T collector is incapable of further upgrading the airflow temperature during these periods due to the insufficiency of solar radiation. However, the $T_{c,out}$ is higher than the $T_{HEX,out}$ in most working hours and peaks at 68.34 °C at noontime. Due to the contribution of the HEX and PV/T collector in terms of airflow temperature upgrading and power generation, less external electricity is consumed by the auxiliary electric heater and thus better performance of the whole system is realised. Overall, the total stored heat and thermal efficiency of the PV/T-TCES-HEX system is 6.64 kWh and 63.61% in the all-day charging process.

5.2. *Performance comparison among three TCES systems*

Thermal efficiency (η_{th}) and external heat input (Q_{in}) are two critical parameters for evaluating the energy storage capacity of a TCES system during the charging process. Fig. 10 shows the thermal efficiency variations of the TCES-only, TCES-HEX, and PV/T-TCES-HEX systems during the one-day charging operation. For all the three systems, the airflow temperature at the inlet of the TCES reactor is maintained constantly at 90 °C, and thus the conversion degree of the hydrated salt and stored heat in the three systems are identical, as presented in Fig. 10 (a) and (b). The conversion degree of the hydrated salt ascends to 0.99 at the end, indicating that most of the salt can be dehydrated within the 12 h. The stored heat of the three TCES systems has a noticeable decrease at the start, then slowly descends from 7:00 to 18:00 with decreasing conversion rates. The thermal efficiency variations of the TCES-only and TCES-HEX systems are similar, with a notable drop at the beginning (i.e., from around 90% to around 22% and 41%, respectively). As shown in Fig. 10 (a), their maximum and average thermal efficiency differences are about 19% and 17%, respectively, which reflects the effect of the involvement of the HEX or not on the system performance. The thermal efficiency of the PV/T-TCES-HEX system also sees a dramatic decline at the beginning and then rises from the bottom (i.e., about 45%) at around 7:00 to a peak (i.e., approximately 85%) at noontime. In general, the PV/T-TCES-HEX system offers higher thermal efficiency than the other two systems during most working hours of the charging process. Particularly, its thermal efficiency is nearly four times that of the TCES-only system and two times that of the TCES-HEX system at noontime. As seen from Fig. 10 (c), the external electricity consumption of the TCES-only system has a slow decrease in the whole charging process. However, the external electricity consumption of the TCES-HEX system sharply drops at the beginning (unsteady state) until it reaches around 1550 W and then slightly decreases in the remaining time. Besides, an average difference in external electricity consumption of 1113.22 W between the TCES-HEX and TCES-only systems is observed, which is attributed to the integration of the HEX. The external energy consumption of the PV/T-TCES-HEX system keeps falling as the solar irradiation increases from 6:00 to 12:00, and then it increases till the end.

The total energy from the PV/T collector, total external electricity consumption, total energy from the PV/T collector and overall thermal efficiency of the three systems are listed in Table 3. The TCES-only system requires 29.26 kWh of external electricity for the entire charging process, while integrating a HEX unit into the TCES system could save nearly half of the electricity input. The total amount of the external electricity consumption required by the PV/T-TCES-HEX system is 11.86 kWh, which is approximately 40.53% and 74.66% of that of the TCES-only and TCES-HEX systems. In the PV/T-TCES-HEX system, the total amount of energy from the PV/T collector is 3.83 kWh, and the power assurance rate of the PV/T collector is 32.32%. Moreover, the overall thermal efficiency of the PV/T-TCES-HEX system reaches 56.00%, corresponding to an improvement of 146.80% and 33.81% compared to the TCES-only and TCES-HEX systems, respectively. Overall, due to the contribution of the HEX and PV/T collector in reducing external power consumption, the thermal efficiency of the PV/T-TCES-HEX system considerably improves during the charging process compared to the TCES-only and TCES-HEX systems.

5.3. *Parametric study*

In this section, the effect of some key operational and structural parameters on the charging performance of the PV/T-TCES-HEX system

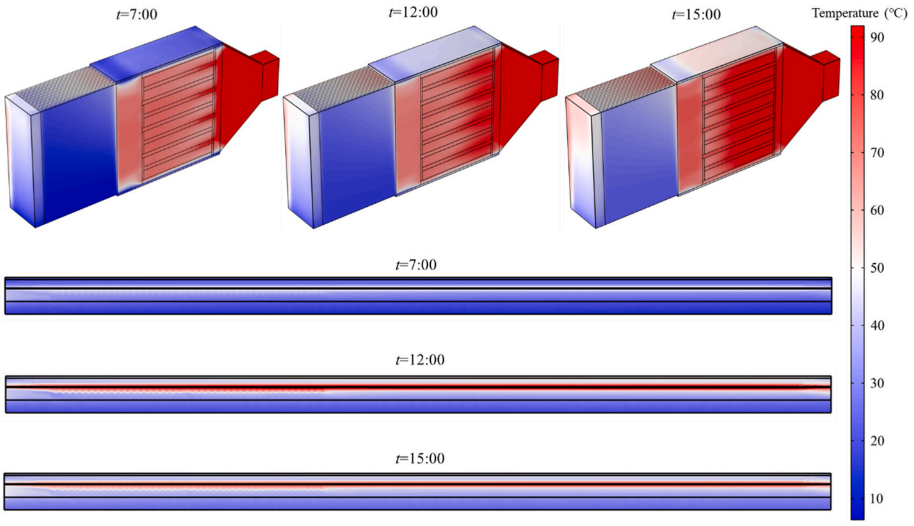

Fig. 9. Temperature distributions of the reactor-HEX and PV/T collector in the PV/T-TCES-HEX system at 7:00, 12:00, and 15:00, respectively.

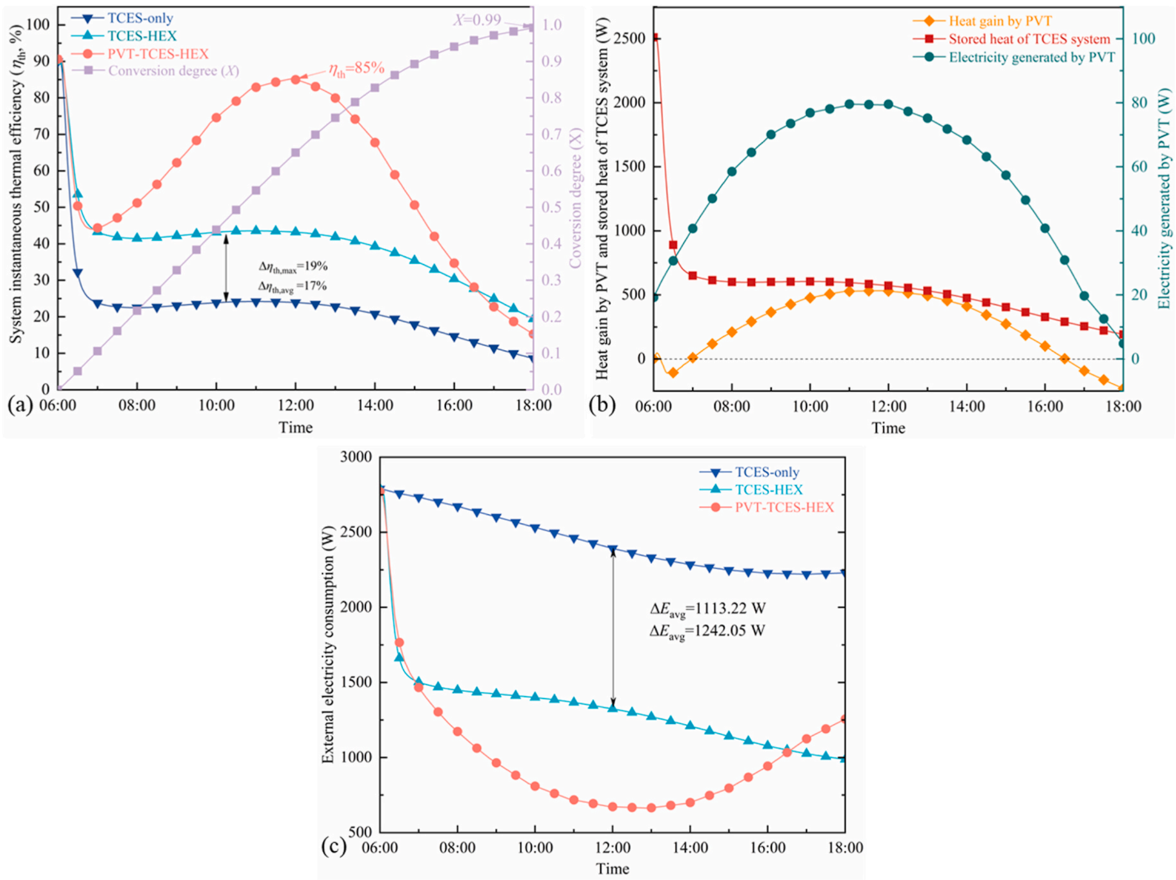

Fig. 10. Comparison of instantaneous thermal efficiency and conversion degree of the PV/T-TCES-HEX, TCES-HEX, and TCES-only systems.

is investigated. The baseline operating conditions (i.e., weather data, reactor structural parameters, system operating parameters, etc.) of the PV/T-TCES-HEX system are mentioned in previous sections.

5.3.1. *Effect of air mass flow rate*

The charging performance of the PV/T-TCES-HEX system under five different air mass flow rates is investigated, and the simulation results are shown in Fig. 11. As seen from Fig. 11 (a), the conversion rate of salt hydrate improves with the increase of the air mass flow rate, as higher air mass flow rates lead to more thermal energy transferred from the airflow to the salt. The conversion rates under all air mass flow rates increase dramatically at the beginning stage, followed by a period of gradual rise until they reach their peak for the system operating at the mass flow rate of 0.04 kg•s^{-1} and 0.035 kg•s^{-1}; others descend slowly in the rest of the charging process as the content of salt hydrates decreases. The maximum conversion rate is 4.08 × 10^{-5} s^{-1} for the system operating at the mass flow rate of 0.04 kg•s^{-1}, nearly twice that at the mass flow rate of 0.02 kg•s^{-1}. Because the salt hydrates are charged faster

Table 3
Total energy from the PV/T collector, total external electricity consumption and overall thermal efficiency of three TCES systems.

	TCES-only	TCES-HEX	PV/T-TCES-HEX
Total energy from the PV/T collector (kWh)	–	–	3.83
Total external electricity consumption (kWh)	29.26	15.86	11.86
Overall thermal efficiency (%)	22.69	41.85	56.00

under a higher air mass flow rate, the salt hydrate conversion rate greatly drops with the increasing air mass flow during the decline phase, as shown in Fig. 11 (a). On the other hand, the amount of heat stored in the systems increases with the air mass flow rate, as shown in Fig. 11 (b). Fig. 11 (c) shows the variations of the external electricity consumption of the systems under the five air mass flow rates. Although higher air mass flow rates indicate better heat transfer coefficients in the HEX and PV/T air channels and thus more heat gains for the airflow when passing through the two components, the airflow temperature at the outlet of the PV/T collector (i.e., the inlet of the auxiliary electric heater) is lower at higher air mass flow rates and more heat input is needed for the airflow to reach 90 °C. In addition, higher mass flow rates require higher fan power. Therefore, more external electricity consumption is demanded with the increase of the air mass flow rate. The bottommost external electricity consumption is 283.46 W for the system operating at the mass flow rate of 0.02 kg•s^{-1}, which is nearly 25% of the input power at the mass flow rate of 0.04 kg•s^{-1}. Fig. 11 (d) presents the thermal efficiency of the PV/T-TCES-HEX system under the five different air mass flow rates. The system has a higher increasing rate in thermal efficiency and a higher peak thermal efficiency at a lower mass flow rate. For instance, the peak thermal efficiency of the system achieves approximately 148.45% when the air mass flow rate is 0.02 kg•s^{-1}, which is more than twice that of the system operating at an air mass flow rate of 0.025 kg•s^{-1}, and the peak thermal efficiency is only 62.31% for the system operating at an air mass flow rate of 0.04 kg•s^{-1}.

It can be noted from Table 4 that a higher air mass flow rate leads to a high conversion degree and total energy from the PV/T collector. An almost complete conversion can be achieved for the air mass flow rate equal to or greater than 0.03 kg•s^{-1}. The total energy from the PV/T collector is 4.25 kWh when the air mass flow rate is 0.04 kg•s^{-1}, which is around 1.2 times that of the system operating at an air mass flow rate

Table 4
Charging performance of the PV/T-TCES-HEX system under different air mass flow rates.

Mass flow rate (kg•s^{-1})	0.02	0.025	0.03	0.035	0.04
Conversion degree (%)	79.48	91.64	99.01	99.73	99.99
Total storage energy (kWh)	5.57	6.24	6.64	6.81	6.85
Total energy from the PV/T collector (kWh)	3.32	3.58	3.83	4.03	4.25
Total external electricity consumption (kWh)	6.96	9.4	11.86	14.42	17.06
Power assurance rate of the PV/T collector (%)	32.32	27.61	24.44	21.86	19.95
Overall thermal efficiency (%)	80.02	66.38	56.00	47.23	40.15

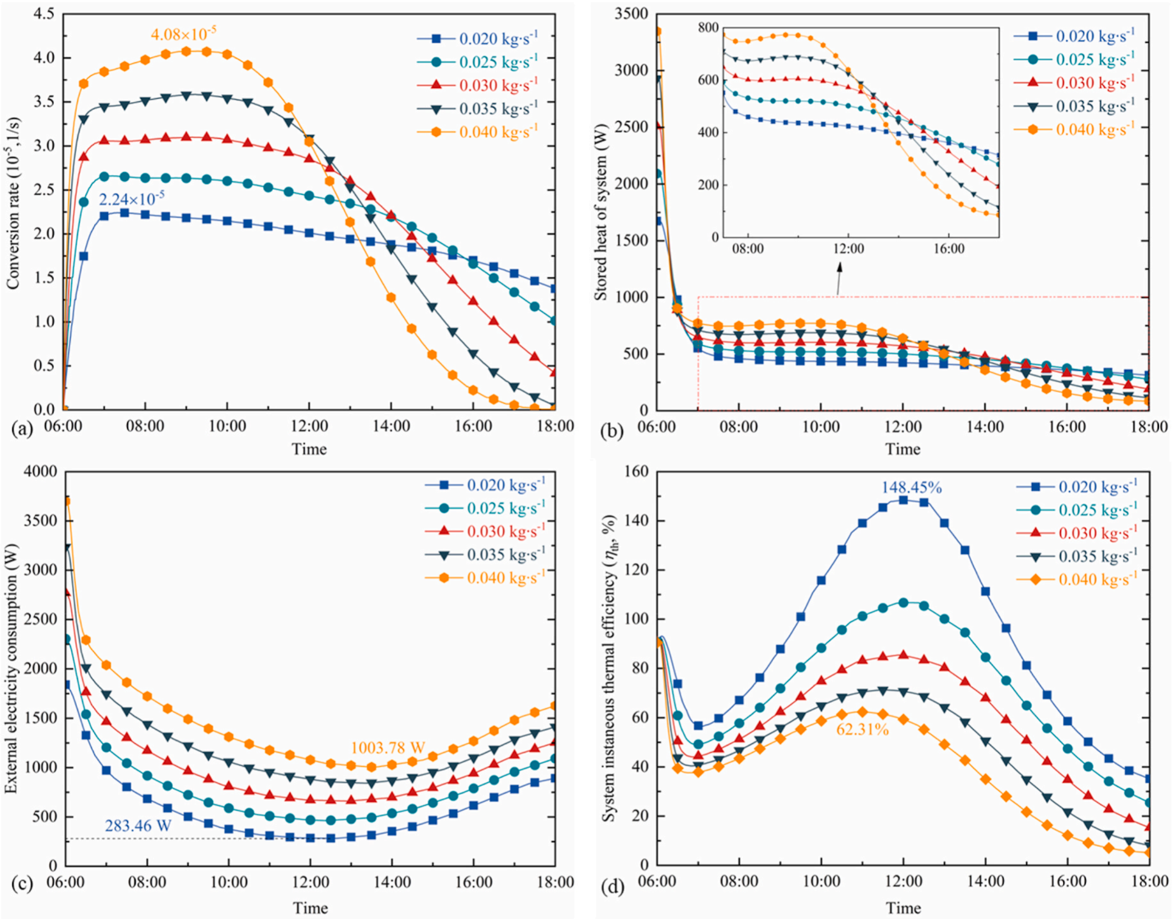

Fig. 11. The change of (a) salt hydrates conversion rate, (b) stored heat, (c) external electricity consumption, and (d) instantaneous thermal efficiency of the PV/T-TCES-HEX system over time under different air mass flow rates.

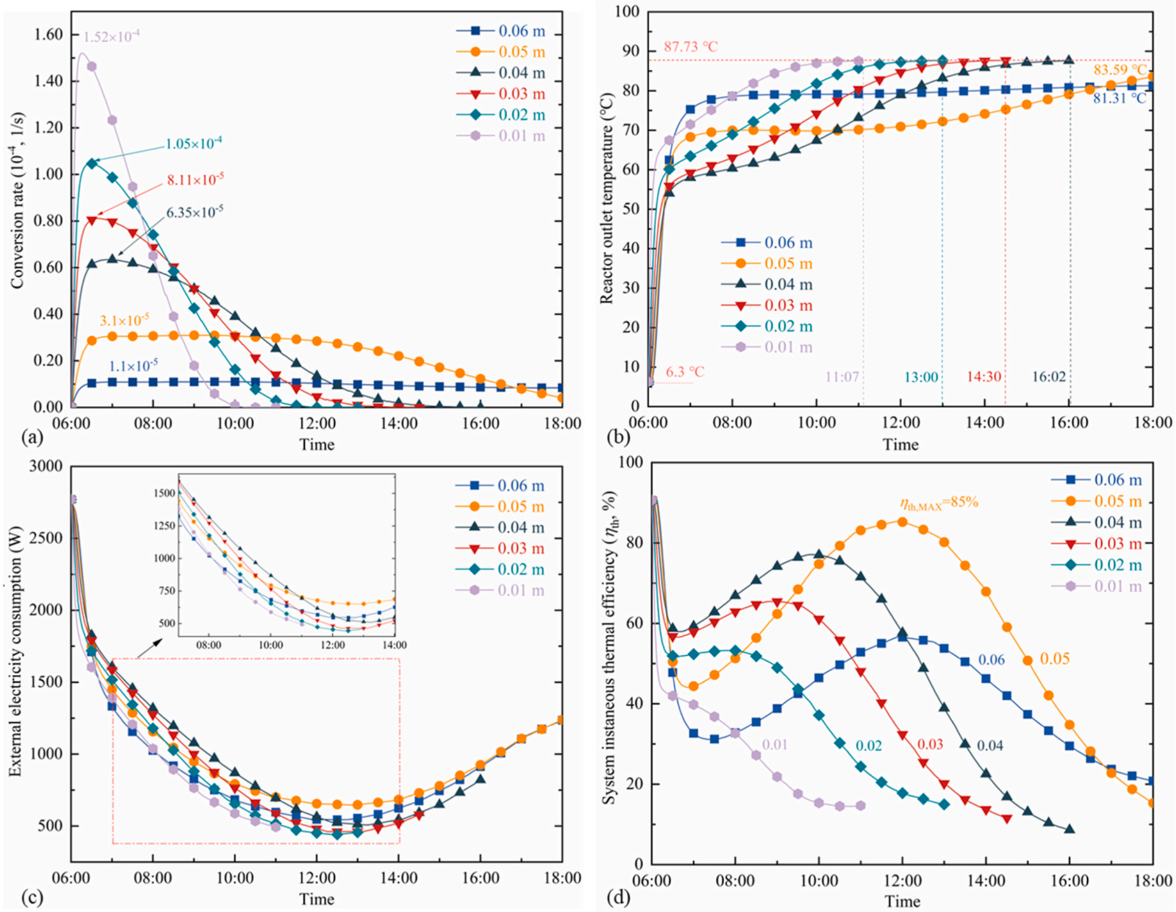

Fig. 12. The variation of (a) salt hydrates conversion rate, (b) airflow temperature at the reactor outlet, (c) external electricity consumption, and (d) instantaneous thermal efficiency of the PV/T-TCES-HEX system over time under different reaction bed thicknesses.

of 0.02 kg•s^{-1}. However, the power assurance rate of the PV/T collector drops from 32.32% to 19.95% when the air mass flow rate increases from 0.02 kg•s^{-1} to 0.04 kg•s^{-1}. The growth of air mass flow leads to faster improvement of external electricity consumption compared to storage energy, therefore decreasing the overall thermal efficiency of the system. In specific, the overall thermal efficiency of the system is 80.02% when the air mass flow rate is 0.02 kg•s^{-1}, which is twice that of the system operating at an air mass flow rate of 0.04 kg•s^{-1} (i.e., 40.15%). The simulation results reveal that increasing the air mass flow rate can improve the conversion rate of the salt hydrate and reduce the time taken for the charging process. However, a higher air mass flow rate results in higher power consumption and lower thermal efficiency.

5.3.2. *Effect of reaction bed thickness*

This section examines the effect of the reaction bed thickness on the charging performance of the PV/T-TCES-HEX system. The simulation results of six different cases are shown in Fig. 12. It can be seen from Fig. 12 (a) that the conversion rate increases with the decrease in the thickness of the reaction bed. They reach their respective maximum at the starting stage of the charging process, and the peaking time point varies with the reactor bed thickness. For instance, at 6:20, the peak of the conversion rate is achieved for the reaction bed with a thickness of 0.01 m, while at 6:30 for the reaction bed with a thickness of 0.02 m. However, there is a significant difference in the maximum conversion rate among the six cases. The maximum conversion rate of the 0.01 m thick reaction bed is around ten times that of the 0.06 m thick reaction bed. According to Fig. 12 (b), the hydrated salts are fully charged at the end for the reaction beds with thicknesses of 0.01 m, 0.02 m, 0.03 m, and 0.04 m, and the corresponding completion time points are 11:07, 13: 00, 14:30, and 16:02, respectively. The airflow temperature at the reactor outlet reaches 87.73 °C upon completion. There is an airflow temperature difference of 2.27 °C between the reactor inlet and outlet, resulting from a part of heat being lost through the reactor wall to the external environment. However, approximately 99% of the hydrated salts are charged for the reaction bed thickness of 0.05 m, and only about 35% of the salts are charged for the reactor bed with a thickness of 0.06 m, and their outlet airflow temperatures are 83.9 °C and 81.3 °C, respectively.

As seen in Fig. 12 (b), the airflow temperature at the outlet of the reactor and PV/T collector does not change regularly with the variation of the reactor bed thickness. The heat absorbed by the TCM during the charging process is directly influenced by the conversion rate and the volume of the reaction bed. A thinner reaction bed offers a higher conversion degree and conversion rate, which leads to an increase in the amount of heat absorbed by the salt hydrate and a reduction in the bed temperature. However, a thinner reaction bed has a smaller TCM volume, causing less heat absorbed and a faster temperature increment. This could explain why the airflow temperature at the reactor outlet varies irregularly under the superimposed influence of the conversion rate and reactor volume with the change in the thickness of the reaction bed. Fig. 12 (c) shows the variation of the external electricity consumption under different reactor bed thicknesses. Because the airflow temperature at the reactor outlet is the most critical factor affecting the external electricity consumption in this case study, the irregular change of the former with the thickness of the bed causes the latter also change irregularly.

The instantaneous thermal efficiency of the system for the six cases is shown in Fig. 12 (d). It can be observed that the increase in the bed thickness results in an improvement in the system thermal efficiency when the bed thickness is below 0.04 m. However, the thermal efficiency of the system with a bed thickness of 0.05 m drops rapidly in the initial phase and is smaller than that of the system with a bed thickness of 0.02 m, 0.03, and 0.04 m between 7:00 and 9:00. The thermal efficiency of the system with a bed thickness of 0.06 m is less than that of the 0.05 m thick reactor bed during most of the charging process as the 0.05 m thick reactor bed absorbs more heat than the 0.06 m thick one.

As shown in Table 5, more energy can be stored in the system with a reactor bed of larger thickness, owing to the increasing TCM volume. Based on the simulation results, the reactor bed with a thickness of 0.05 m offers the best energy storage performance and PV/T power supply, with which in total 6.64 kWh energy is stored and 3.83 kWh energy is provided by the PV/T collector. In terms of thermal performance, the reactor bed with a thickness of 0.04 m exhibits the highest overall system thermal efficiency (i.e., 57.55%). Simultaneously, it shows the highest power assurance rate of the PV/T collector (i.e., 28.45%). The simulation results indicate the importance of optimising the reactor design to improve the overall performance of the PV/T-TCES-HEX system.

5.3.3. *Effect of reaction bed length*

In addition, the effect of reaction bed length on the charging performance of the PV/T-TCES-HEX system is assessed, and the simulated results are shown in Fig. 13. The conversion rate of the salt hydrate increases with the decrement in the length of the reaction bed, as shown in Fig. 13 (a). The maximum conversion rate peaks at 4.07×10^{-5} s^{-1} when the length of the reaction bed is 0.3 m, which is approximately twice that of the 0.5 m length case. The change in stored heat and external electricity consumption are presented in Fig. 13 (b) and (c), respectively. It can be seen that the stored heat and external power consumption vary non-monotonically with the change in the length of the reaction bed, which is because the stored heat of the system is affected by both the conversion rate and content of salt hydrate. Affected by stored heat and external power consumption, the instantaneous thermal efficiency of the system also demonstrates irregular variations, as seen in Fig. 13 (d).

The charging performance of the PV/T-TCES-HEX system under different reaction bed lengths is summarized in Table 6. The system with a reaction bed length of 0.5 m shows the best performance in the all-day charging process, with the total storage energy and thermal efficiency of 7.07 kWh and 58.73%, respectively, corresponding to a 6% and 4% improvement roughly compared to the reference length case (i.e., 0.4 m). Simultaneously, the maximum amount of energy (3.88 kWh) is provided by the PV/T collector when the bed length is 0.5 m. However, the power assurance rate of the PV/T collector remains at around 24% in the five bed-length cases. The increase in the reaction bed length leads to faster decline of storage energy compared to external electricity consumption when the reaction length exceeds 0.5 m, therefore resulting in a decrement in the overall thermal efficiency of the system.

6. Conclusions

In this study, a solar-driven thermochemical energy storage (TCES) system combined with a heat recovery unit (heat exchanger, HEX) and a PV/T collector (PV/T-TCES-HEX system) is proposed. A mathematical model is developed, and simulations are conducted using COMSOL to investigate the charging performance of the proposed system operating on a typical summer day in Nottingham, UK. Performance comparisons are implemented for the PV/T-TCES-HEX system with a system combining a TCES reactor and a heat exchanger (TCES-HEX system) and a stand-alone TCES system (TCES-only system). A parametric study is carried out to evaluate the effect of different parameters on the system performance. The following conclusions can be drawn.

Table 5
Charging performance of the PV/T-TCES-HEX system under different reaction bed thicknesses.

Reaction bed thickness (m)	0.01	0.02	0.03	0.04	0.05	0.06
Conversion degree	1	1	1	1	0.99	0.35
Total energy from the PV/T collector (kWh)	1.23	2.33	3.11	3.61	3.83	3.29
Total external electricity consumption (kWh)	5.09	6.53	7.88	9.55	11.86	11.01
Total storage energy (kWh)	1.71	3.03	4.26	5.50	6.64	4.61
Power assurance rate of the PV/T collector (%)	19.60	26.40	27.69	28.45	24.71	23.38
Overall thermal efficiency (%)	33.66	46.39	54.09	57.55	56.00	41.85

(1) An average airflow temperature difference of 33.44 °C between the HEX outlet and system inlet of the PV/T-TCES-HEX system is observed during the charging process, demonstrating that the integration of the HEX leads to effective heat recovery to the system. The total stored heat and thermal efficiency of the PV/T-TCES-HEX system is 6.64 kWh and 63.61% in the all-day charging process.

(2) Integrating the HEX and PV/T collector into the TCES system can contribute to the reduction in the required external electricity consumption and the increase in the system thermal efficiency. The PV/T-TCES-HEX system requires an external electricity consumption of 11.86 kWh, which is 67.39% and 36.54% of that of the TCES-HEX and TCES-only systems, respectively. The overall thermal efficiency of the PV/T-TCES-HEX system is 56.00%, which is respectively 33.81% and 146.80% greater than that of the TCES-HEX and TCES-only systems.

(3) A higher air mass flow rate contributes to a higher conversion degree at the cost of more external electricity consumption and therefore leads to a lower overall thermal efficiency of the PV/T-TCES-HEX system. The overall thermal efficiency of the system is 80.02% under an air mass flow rate of 0.02 $kg•s^{-1}$, which is about twice that under an air mass flow rate of 0.04 $kg•s^{-1}$.

(4) Since the thermochemical reaction of the system is affected by both the conversion rate and content of salt hydrate, the length and thickness of the reaction bed show non-monotonic effects on the charging performance of the PV/T-TCES-HEX system. The reactor bed with a thickness of 0.05 m provides the highest energy storage capacity (i.e., 6.64 kWh), and the reactor bed with a thickness of 0.04 m offers the highest total system thermal efficiency (i.e., 57.55%). Besides, the system with a reaction bed length of 0.5 m shows the best charging performance, with the total energy storage capacity and thermal efficiency being 7.07 kWh and 58.73%, respectively.

Overall, the proposed PV/T-TCES-HEX system provides an effective solution to improve the thermochemical energy storage performance during the charging phase by harvesting solar heat and waste heat from the TCES reactor. It is worth noting that, the airflow temperature is heated up to the set point before entering into the TCES reactor by an electric heater for analysis simplicity as the emphasis of this feasibility study is to investigate the effect of the heat recovery unit and PV/T collector. In future work, more energy-efficient device such as a heat pump can be introduced to replace the electric heater for further performance improvement. In addition, further structural optimizations of the reactor bed and PV/T air channel will be carried out to realize better thermal performance of the PV/T-TCES-HEX system. The charging performance of the PV/T-TCES-HEX system under dynamic airflow temperatures at the reactor inlet and different climatic regions will also be evaluated.

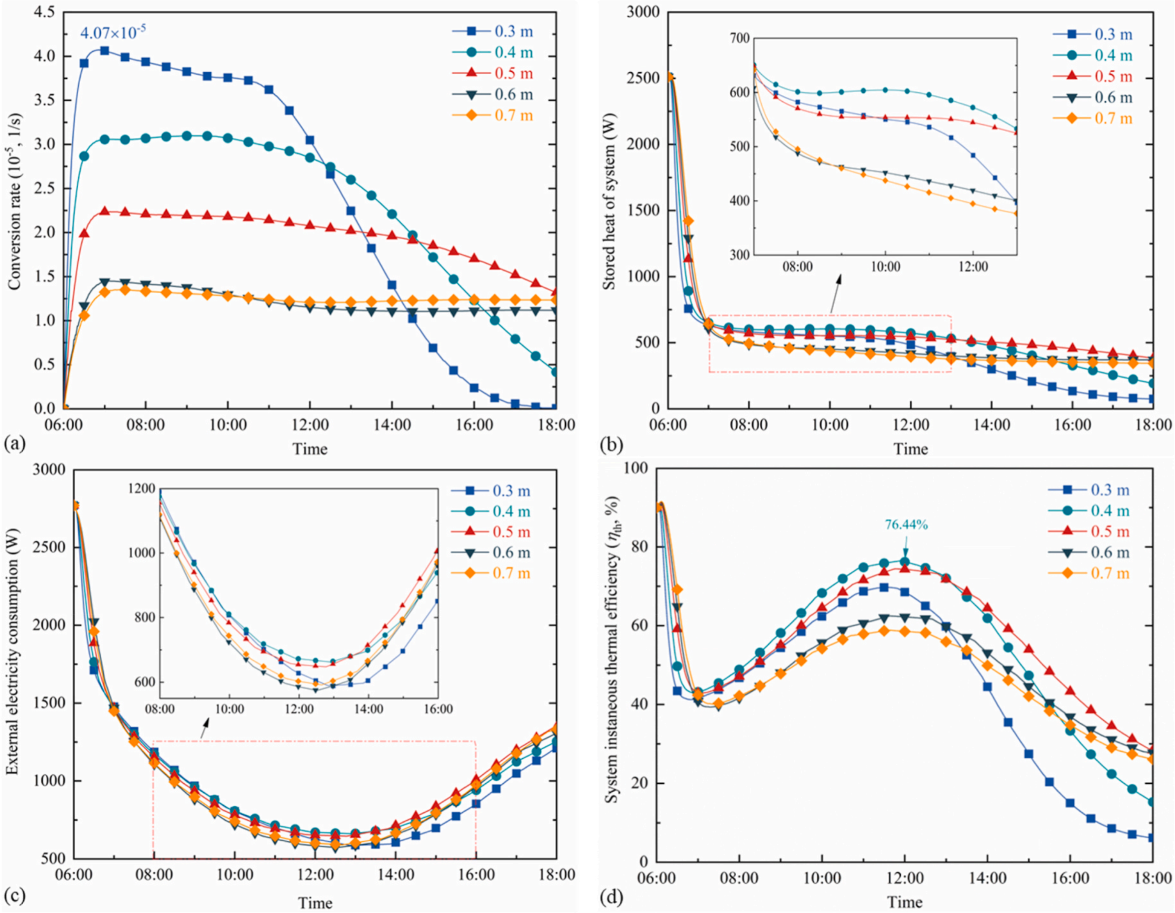

Fig. 13. The change of (a) salt hydrates conversion rate, (b)stored heat, (c) external electricity consumption, and (d) system instantaneous thermal efficiency over time under different reaction bed lengths.

CRediT authorship contribution statement

Yong Zhang: Software, Formal analysis, Investigation, Writing – original draft, Writing – review & editing. **Mingke Hu:** Conceptualization, Supervision, Methodology, Formal analysis, Investigation, Writing – review & editing. **Ziwei Chen:** Formal analysis, Writing – review & editing. **Yuehong Su:** Conceptualization, Supervision, Project administration, Funding acquisition, Writing – review & editing. **Saffa Riffat:** Resources, Project administration, Writing – review & editing.

Declaration of competing interest

The authors declare that they have no known competing financial interests or personal relationships that could have appeared to influence the work reported in this paper.

Data availability

Data will be made available on request.

Acknowledgements

The authors would like to acknowledge the Engineering and Physical Sciences Research Council (grant number: EP/T021233/1) for the financial support to this research.

Table 6
Charging performance of the PV/T-TCES-HEX system under different reaction bed lengths.

Reaction bed length (m)	0.3	0.4	0.5	0.6	0.7
Conversion degree	0.99	0.97	0.8	0.48	0.49
Total energy from the PV/T collector (kWh)	3.62	3.84	3.88	3.74	3.71
Total external electricity consumption (kWh)	11.30	11.86	12.04	11.79	11.49
Total storage energy (kWh)	5.31	6.64	7.07	6.53	5.83
The power assurance rate of the PV/T collector	24.25	24.45	24.39	24.45	24.39
Overall thermal efficiency (%)	46.96	56.00	58.73	54.31	50.68

Nomenclature

A	Area, m^2
A_{freq}	Pre-exponential Arrhenius factor, s^{-1}
B	Temperature coefficient of PV cells, K^{-1}
C	Specific heat, J•kg^{-1}•K^{-1}
c	Mole concentration, mol•m^{-3}
D_g	Gas diffusivity in reactive bed, m^2•s^{-1}
d	Thickness or depth, m
E	Electrical power, W
E_a	Arrhenius activation energy, J•mol^{-1}
G	Solar irradiance, W•m^{-2}

H	Enthalpy, J
h	Heat transfer coefficient, W•m^{-2}•K^{-1}
k	Thermal conductivity, W•m^{-1}•K^{-1}
M	Molecular mass, g•mol^{-1}
$\dot{m}$Mass flow rate, kg•s^{-1}Nu Mass flow rate, kg•s^{-1}NuNusselt number	
P	Pressure, Pa
PAR	Power assurance rate, %
Pr	Prandtl number
$\dot{q}$Volume power source, W•m^{-3}Q Volume power source, W•m^{-3}QHeat	
R	Ideal gas constant, J•mol^{-1}•K^{-1}
Ra	Rayleigh number
R_{kin}	Kinetic factor, s^{-1}
R_{th}	Thermal resistance, m^2·K•W^{-1}
S	Entropy, J•mol^{-1}•K^{-1}
S_{w}	Mass source of water vapour, kg•m^{-3}·s^{-1}
T	Temperature, K or °C
t	Time, s
$\vec{u}$Velocity vector, m•s^{-1}V Velocity vector, m•s^{-1}VVolume of salt bed, m^3	
X	Reaction conversion degree, %
z	Stoichiometric number

Greek symbols

ρ	Density or reflectivity, kg•m^{-3} or
τ	Transmissivity
$(\tau\alpha)$	Transmissivity–absorptivity product
α	Absorptivity
ε	Emissivity
σ	Stefan–Boltzmann constant
β	Inclination angle, °
ξ	Packing factor
η	Efficiency
δ	Porosity of the salt bed
φ	Permeability, m^2
γ	Volume flow rate, m^3•s^{-1}

Subscripts

a	Air
Al	Aluminium substrate
ch	Charging
eff	Effective
eq	Equilibrium state
f	Final
fan	Air fan
g	Glass cover
i	Initial
in	Inlet
ins	Insulation plate
ind	Indoor air
kin	Kinetic
out	Outlet
PV	PV module
r	Reactor
ref	Reference
s	Salt hydrate
sys	System
th	Thermal
v	Water vapour

References

[1] Global primary energy consumption 2021 | Statista, (n.d.). https://www.statista.com/statistics/265598/consumption-of-primary-energy-worldwide/ (accessed November 8, 2022).

[2] Digest of UK Energy Statistics (DUKES) 2021 - GOV.UK, (n.d.). https://www.gov.uk/government/statistics/digest-of-uk-energy-statistics-dukes-2021 (accessed October 23, 2022).

[3] I. - International Energy Agency, ENERGY POLICIES OF IEA COUNTRIES Together Secure Sustainable, (n.d.). www.iea.org/t&c/ (accessed June 8, 2022).

[4] National Energy Action (NEA} Policy Briefing | Energy Crisis, (n.d.). https://www.nea.org.uk/energy-crisis/supporting-vulnerable-energy-customers-through-the-energy-crisis/ (accessed October 23, 2022).

[5] I. Stewart, P. Bolton, Domestic energy prices, (n.d.). https://commonslibrary.parliament.uk/research-briefings/cbp-9491/ (accessed October 22, 2022).

[6] D. Aydin, S.P. Casey, S. Riffat, The latest advancements on thermochemical heat storage systems, Renew. Sustain. Energy Rev. 41 (2015) 356–367, https://doi.org/10.1016/J.RSER.2014.08.054.

[7] R. Han, S. Xing, X. Wu, C. Pang, S. Lu, Y. Su, Q. Liu, C. Song, J. Gao, Relevant influence of alkali carbonate doping on the thermochemical energy storage of Ca-based natural minerals during CaO/CaCO3 cycles, Renew. Energy 181 (2022) 267–277, https://doi.org/10.1016/J.RENENE.2021.09.021.

[8] Z. Ding, W. Wu, M. Leung, Advanced/hybrid thermal energy storage technology: material, cycle, system and perspective, Renew. Sustain. Energy Rev. 145 (2021), 111088, https://doi.org/10.1016/J.RSER.2021.111088.

[9] P. Ammendola, F. Raganati, F. Miccio, A.N. Murri, E. Landi, Insights into utilization of strontium carbonate for thermochemical energy storage, Renew. Energy 157 (2020) 769–781, https://doi.org/10.1016/J.RENENE.2020.05.048.

[10] D. Mahon, P. Henshall, G. Claudio, P.C. Eames, Feasibility study of MgSO4 + zeolite based composite thermochemical energy stores charged by vacuum flat plate solar thermal collectors for seasonal thermal energy storage, Renew. Energy 145 (2020) 1799–1807, https://doi.org/10.1016/J.RENENE.2019.05.135.

[11] B. Michel, N. Mazet, S. Mauran, D. Stitou, J. Xu, Thermochemical process for seasonal storage of solar energy: characterization and modeling of a high density reactive bed, Energy 47 (2012) 553–563, https://doi.org/10.1016/J.ENERGY.2012.09.029.

[12] Z. Ma, H. Bao, A.P. Roskilly, Electricity-assisted thermochemical sorption system for seasonal solar energy storage, Energy Convers. Manag. 209 (2020), 112659, https://doi.org/10.1016/J.ENCONMAN.2020.112659.

[13] A.H. Abedin, A critical review of thermochemical energy storage systems, Open Renew. Energy J. 4 (2011) 42–46, https://doi.org/10.2174/1876387101004010042.

[14] M. Yekini Suberu, M. Wazir Mustafa, N. Bashir, Energy storage systems for renewable energy power sector integration and mitigation of intermittency, Renew. Sustain. Energy Rev. 35 (2014) 499–514, https://doi.org/10.1016/J.RSER.2014.04.009.

[15] W. Chen, W. Li, Y. Zhang, Analysis of thermal deposition of MgCl2·6H2O hydrated salt in the sieve-plate reactor for heat storage, Appl. Therm. Eng. 135 (2018) 95–108, https://doi.org/10.1016/J.APPLTHERMALENG.2018.02.043.

[16] K. Heijmans, S. Nab, B. Klein Holkenborg, A.D. Pathak, S. Gaastra-Nedea, D. Smeulders, Development of a reactive force field for CaCl2·nH2O, and the application to thermochemical energy storage, Comput. Mater. Sci. 197 (2021), 110595, https://doi.org/10.1016/J.COMMATSCI.2021.110595.

[17] Q. Miao, Y. Zhang, X. Jia, L. Tan, Y. Ding, MgSO4-expanded graphite composites for mass and heat transfer enhancement of thermochemical energy storage, Sol. Energy 220 (2021) 432–439, https://doi.org/10.1016/J.SOLENER.2021.03.008.

[18] A. Fopah-Lele, J.G. Tamba, A review on the use of SrBr2·6H2O as a potential material for low temperature energy storage systems and building applications, Sol. Energy Mater. Sol. Cell. 164 (2017) 175–187, https://doi.org/10.1016/J.SOLMAT.2017.02.018.

[19] K.E. N'Tsoukpoe, T. Schmidt, H.U. Rammelberg, B.A. Watts, W.K.L. Ruck, A systematic multi-step screening of numerous salt hydrates for low temperature thermochemical energy storage, Appl. Energy 124 (2014) 1–16, https://doi.org/10.1016/j.apenergy.2014.02.053.

[20] A. Fopah-Lele, J.G. Tamba, A review on the use of SrBr2·6H2O as a potential material for low temperature energy storage systems and building applications, Sol. Energy Mater. Sol. Cell. 164 (2017) 175–187, https://doi.org/10.1016/J.SOLMAT.2017.02.018.

[21] A.U. Rehman, M. Khan, Z. Maosheng, Hydration behavior of MgSO4–ZnSO4 composites for long-term thermochemical heat storage application, J. Energy Storage 26 (2019), 101026, https://doi.org/10.1016/J.EST.2019.101026.

[22] Q. Touloumet, L. Silvester, L. Bois, G. Postole, A. Auroux, Water sorption and heat storage in CaCl2 impregnated aluminium fumarate MOFs, Sol. Energy Mater. Sol. Cell. 231 (2021), 111332, https://doi.org/10.1016/J.SOLMAT.2021.111332.

[23] A.I. Shkatulov, J. Houben, H. Fischer, H.P. Huinink, Stabilization of K2CO3 in vermiculite for thermochemical energy storage, Renew. Energy 150 (2020) 990–1000, https://doi.org/10.1016/J.RENENE.2019.11.119.

[24] Q. Wang, Y. Xie, B. Ding, G. Yu, F. Ye, C. Xu, Structure and hydration state characterizations of MgSO4-zeolite 13x composite materials for long-term thermochemical heat storage, Sol. Energy Mater. Sol. Cell. 200 (2019), 110047, https://doi.org/10.1016/J.SOLMAT.2019.110047.

[25] B. Ding, C. Xu, Z. Liao, F. Ye, Study on long-term thermochemical thermal storage performance based on SrBr2-expanded vermiculite composite materials, J. Energy Storage 42 (2021), https://doi.org/10.1016/j.est.2021.103081.

[26] W. Li, J.J. Klemeš, Q. Wang, M. Zeng, Energy storage of low potential heat using lithium hydroxide based sorbent for domestic heat supply, J. Clean. Prod. 285 (2021), 124907, https://doi.org/10.1016/J.JCLEPRO.2020.124907.

[27] W. Li, J.J. Klemeš, Q. Wang, M. Zeng, Development and characteristics analysis of salt-hydrate based composite sorbent for low-grade thermochemical energy storage, Renew. Energy 157 (2020) 920–940, https://doi.org/10.1016/J.RENENE.2020.05.062.

[28] Y.J. Zhao, R.Z. Wang, Y.N. Zhang, N. Yu, Development of SrBr2 composite sorbents for a sorption thermal energy storage system to store low-temperature heat, Energy 115 (2016) 129–139, https://doi.org/10.1016/J.ENERGY.2016.09.013.

[29] S. Mauran, H. Lahmidi, V. Goetz, Solar heating and cooling by a thermochemical process. First experiments of a prototype storing 60 kW h by a solid/gas reaction, Sol. Energy 82 (2008) 623–636, https://doi.org/10.1016/j.solener.2008.01.002.

[30] A. Ristić, S.K. Henninger, Sorption composite materials for solar thermal energy storage, Energy Proc. 48 (2014) 977–981, https://doi.org/10.1016/J.EGYPRO.2014.02.111.

[31] E. Courbon, P. D'Ans, A. Permyakova, O. Skrylnyk, N. Steunou, M. Degrez, M. Frère, A new composite sorbent based on SrBr2 and silica gel for solar energy storage application with high energy storage density and stability, Appl. Energy 190 (2017) 1184–1194, https://doi.org/10.1016/J.APENERGY.2017.01.041.

[32] Y.N. Zhang, R.Z. Wang, Y.J. Zhao, T.X. Li, S.B. Riffat, N.M. Wajid, Development and thermochemical characterizations of vermiculite/SrBr2 composite sorbents for low-temperature heat storage, Energy 115 (2016) 120–128, https://doi.org/10.1016/J.ENERGY.2016.08.108.

[33] Q. Zhao, J. Lin, H. Huang, Q. Wu, Y. Shen, Y. Xiao, Optimization of thermochemical energy storage systems based on hydrated salts: a review, Energy Build. 244 (2021), 111035, https://doi.org/10.1016/J.ENBUILD.2021.111035.

[34] A. Fopah-Lele, C. Rohde, K. Neumann, T. Tietjen, T. Rönnebeck, K.E. N'Tsoukpoe, T. Osterland, O. Opel, W.K.L. Ruck, Lab-scale experiment of a closed thermochemical heat storage system including honeycomb heat exchanger, Energy 114 (2016) 225–238, https://doi.org/10.1016/j.energy.2016.08.009.

[35] B. Michel, N. Mazet, P. Neveu, Experimental investigation of an innovative thermochemical process operating with a hydrate salt and moist air for thermal storage of solar energy: global performance, Appl. Energy 129 (2014) 177–186, https://doi.org/10.1016/J.APENERGY.2014.04.073.

[36] H. Zhang, S. Liu, A. Shukla, Y. Zou, X. Han, Y. Shen, L. Yang, P. Zhang, K. Kusakana, Thermal performance study of thermochemical reactor using net-packed method, Renew. Energy 182 (2022) 483–493, https://doi.org/10.1016/J.RENENE.2021.09.115.

[37] W. Li, H. Guo, M. Zeng, Q. Wang, Performance of SrBr2·6H2O based seasonal thermochemical heat storage in a novel multilayered sieve reactor, Energy Convers. Manag. 198 (2019), https://doi.org/10.1016/j.enconman.2019.111843.

[38] A. Fopah Lele, F. Kuznik, O. Opel, W.K.L. Ruck, Performance analysis of a thermochemical based heat storage as an addition to cogeneration systems, Energy Convers. Manag. 106 (2015) 1327–1344, https://doi.org/10.1016/j.enconman.2015.10.068.

[39] W. Chen, W. Li, Y. Zhang, Analysis of thermal deposition of MgCl2·6H2O hydrated salt in the sieve-plate reactor for heat storage, Appl. Therm. Eng. 135 (2018) 95–108, https://doi.org/10.1016/j.applthermaleng.2018.02.043.

[40] A. Mukherjee, R. Majumdar, S.K. Saha, C. Subramaniam, L. Kumar, Performance evaluation of an open thermochemical energy storage system integrated with flat plate solar collector, Appl. Therm. Eng. 173 (2020), https://doi.org/10.1016/j.applthermaleng.2020.115218.

[41] A. Mukherjee, A. Shankar Pujari, S.N. Shinde, U. Kashyap, L. Kumar, C. Subramaniam, S.K. Saha, Performance assessment of open thermochemical energy storage system for seasonal space heating in highly humid environment, Renew. Energy 201 (2022) 960–1481, https://doi.org/10.1016/j.renene.2022.10.075.

[42] J. Lin, Q. Zhao, H. Huang, H. Mao, Y. Liu, Y. Xiao, Applications of low-temperature thermochemical energy storage systems for salt hydrates based on material classification: a review, Sol. Energy 214 (2021) 149–178, https://doi.org/10.1016/J.SOLENER.2020.11.055.

[43] A.H. Abedin, M.A. Rosen, Closed and open thermochemical energy storage: energy- and exergy-based comparisons, Energy 41 (2012) 83–92, https://doi.org/10.1016/J.ENERGY.2011.06.034.

[44] F. Trausel, A.J. de Jong, R. Cuypers, A review on the properties of salt hydrates for thermochemical storage, Energy Proc. 48 (2014) 447–452, https://doi.org/10.1016/J.EGYPRO.2014.02.053.

[45] B. Michel, P. Neveu, N. Mazet, Comparison of closed and open thermochemical processes, for long-term thermal energy storage applications, Energy 72 (2014) 702–716, https://doi.org/10.1016/J.ENERGY.2014.05.097.

[46] A. Malley-Ernewein, S. Lorente, Constructal design of thermochemical energy storage, Int. J. Heat Mass Tran. 130 (2019) 1299–1306, https://doi.org/10.1016/J.IJHEATMASSTRANSFER.2018.10.097.

[47] C. Guo, J. Ji, W. Sun, J. Ma, W. He, Y. Wang, Numerical simulation and experimental validation of tri-functional photovoltaic/thermal solar collector, Energy 87 (2015) 470–480, https://doi.org/10.1016/J.ENERGY.2015.05.017.

[48] H. Liu, K. Nagano, Numerical simulation of an open sorption thermal energy storage system using composite sorbents built into a honeycomb structure, Int. J. Heat Mass Tran. 78 (2014) 648–661, https://doi.org/10.1016/J.IJHEATMASSTRANSFER.2014.07.034.

[49] A. Fopah Lele, F. Kuznik, H.U. Rammelberg, T. Schmidt, W.K.L. Ruck, Thermal decomposition kinetic of salt hydrates for heat storage systems, Appl. Energy 154 (2015) 447–458, https://doi.org/10.1016/j.apenergy.2015.02.011.

[50] S.P. Casey, J. Elvins, S. Riffat, A. Robinson, Salt impregnated desiccant matrices for 'open' thermochemical energy storage—selection, synthesis and characterisation of candidate materials, Energy Build. 84 (2014) 412–425, https://doi.org/10.1016/J.ENBUILD.2014.08.028.

[51] J.H. Watmuff, W.W.S. Charters, D. Proctor, J.H. Watmuff, W.W.S. Charters, D. Proctor, Solar and wind induced external coefficients - solar collectors, Cmes (1977) 56. https://ui.adsabs.harvard.edu/abs/1977cmes.rept...56W/abstract. (Accessed 30 October 2022).

[52] M. Hu, B. Zhao, X. Ao, X. Ren, J. Cao, Q. Wang, Y. Su, G. Pei, Performance assessment of a trifunctional system integrating solar PV, solar thermal, and radiative sky cooling, Appl. Energy 260 (2020), 114167, https://doi.org/10.1016/J.APENERGY.2019.114167.

[53] P. Gang, F. Huide, Z. Huijuan, J. Jie, Performance study and parametric analysis of a novel heat pipe PV/T system, Energy 37 (2012) 384–395, https://doi.org/10.1016/J.ENERGY.2011.11.017.

[54] F.P. Incropera, D.P. DeWitt, T.L. Bergman, A.S. Lavine, Fundamentals of Heat and Mass Transfer-Incropera, 2011, pp. 400–402. https://books.google.com/books/about/Fundamentals_of_Heat_and_Mass_Transfer.html?hl=zh-CN&id=vvyIoXEywMoC. (Accessed 30 October 2022).

[55] X. Ren, J. Li, M. Hu, G. Pei, D. Jiao, X. Zhao, J. Ji, Feasibility of an innovative amorphous silicon photovoltaic/thermal system for medium temperature applications, Appl. Energy 252 (2019), 113427, https://doi.org/10.1016/J.APENERGY.2019.113427.

[56] Greenheck Product Application Guide-Understanding Fan Efficiency Grades, (FEG) (2013). https://content.greenheck.com/public/DAMProd/Original/10002/CS104-13_FEG.pdf (accessed November 11, 2022).

[57] J. Ji, C. Guo, W. Sun, W. He, Y. Wang, G. Li, Experimental investigation of tri-functional photovoltaic/thermal solar collector, Energy Convers. Manag. 88 (2014) 650–656, https://doi.org/10.1016/J.ENCONMAN.2014.09.030.

[58] H. Bahaidarah, A. Subhan, P. Gandhidasan, S. Rehman, Performance evaluation of a PV (photovoltaic) module by back surface water cooling for hot climatic conditions, Energy 59 (2013) 445–453, https://doi.org/10.1016/J.ENERGY.2013.07.050.

[59] climate.onebuilding.org, (n.d.). https://climate.onebuilding.org/default.html (accessed November 14, 2022).